1   Stratospheric circulation response to large Northern high-latitude volcanic eruptions.

2

3   Hera Guðlaugsdóttir[1,2], Yannick Peings[2], Davide Zanchettin[3], Gudrun Magnusdottir[2]

4   [1]University of Iceland, institute of Earth Sciences, 102 Reykjavík, Iceland

5   [2]University of California Irvine, Department of Earth System Science, Irvine CA 92697-3100,

6   United States

7   [3]University Ca'Foscari of Venice, department of Environmental Sciences, Informatics and

8   Statistics, 30123 Venice, Italy

9   *Correspondence to:* Hera Guðlaugsdóttir (hera@hi.is)

10

11

12

13

14   Abstract

15   The temporary enhancement of the stratospheric aerosol layer after major explosive volcanic eruptions can

16   trigger climate anomalies for up to several years following such events. Whereas the mechanisms

17   responsible for the prolonged response to volcanic surface cooling have been extensively investigated for

18   tropical eruptions, less is known about the dynamical response to high-latitude eruptions. Here we use

19   global climate model simulations of an idealized 6 month long northern hemisphere high-latitude eruption

20   to investigate the stratospheric circulation response during the first three post-eruption winters. Two model

21   configurations are used, with an interactive ocean, or with prescribed sea surface temperature. Our results

22   reveal significant differences in the response of the polar stratosphere with an interactive ocean: the surface

23   cooling is enhanced and zonal flow anomalies are stronger in the troposphere, which impacts atmospheric

24   waveguides and upward propagation of large-scale planetary waves. We identify two competing

25   mechanisms contributing to the post-eruption evolution of the polar vortex: 1) A local stratospheric top-

26   down mechanism whereby increased absorption of aerosol-induced thermal radiation yields a polar vortex

27   strengthening via thermal wind response; 2) A bottom-up mechanism whereby anomalous surface cooling

28   yields a wave-activity flux increase that propagates into the winter stratosphere. This causes a weakening

29   of the polar vortex and an increase in the occurrence of sudden stratospheric warming events (SSWs),

30   although with a small signal-to-noise ratio. In the coupled runs, the top-down mechanism dominates over

31   the bottom-up mechanism in winter 1, while the bottom-up mechanism dominates in the follow-up winters.

32

33

1 Introduction

The enhancement of the stratospheric aerosol layer, which typically occurs following strong sulfur-rich explosive volcanic eruptions, is an important driver of natural climate variability by imposing short-lived yet possibly very strong radiative anomalies within the atmospheric column (Robock, 2000; Timmreck, 2012; Zanchettin, 2017). This direct radiative effect can alter both meridional surface and stratospheric temperature gradients that can, in turn, initiate further dynamical climate responses on seasonal to decadal time scales (Church et al., 2005; Gleckler et al., 2006; Stenchikov et al., 2009; Shindell et al., 2009; Otterå et al., 2010; Zanchettin et al., 2012; Swingedouw et al., 2015). Direct radiative and dynamical responses critically depend on the spatiotemporal characteristics of the enhanced stratospheric aerosol layer, which ultimately depends on the characteristics of the eruption, such as magnitude, timing and location (Stenchikov et al., 2009; Shindell et al., 2009; Zanchettin et al., 2012; Swingedouw et al., 2015). Spatiotemporal characteristics of volcanic aerosol from high-latitude (HL), Northern Hemisphere (NH) eruptions are typically very different when compared to tropical eruptions. Accordingly, several studies have shown that high-latitude NH eruptions typically initiate different climate responses compared to tropical eruptions (Meronen et al., 2012; Pausata et al., 2015; Guðlaugsdóttir et al., 2018; Zambri et al., 2019; Sjolte et al., 2021). Therefore, tropical eruptions cannot be considered close analogs of high-latitude NH eruptions, underlining the need for more studies on the latter to further quantify their potential climate impacts (Zanchettin et al., 2016). In this study we explore how stratospheric sulfate aerosol enhancements largely constrained in the NH extratropics affect hemispheric-scale atmospheric dynamics, with a focus on the stratospheric polar vortex and on temporal evolution of responses through three perturbed winters.

The winter stratospheric polar vortex is considered to play a deciding role in distinguishing between the response to low- and high-latitude NH enhancements of the stratospheric sulfate aerosol layer, where opposite responses are expected to emerge under the same mechanism: When the stratospheric sulfate aerosol layer is enhanced at low latitudes, e.g., following tropical volcanic eruptions, local warming by infrared absorption increases the meridional stratospheric temperature gradient that can lead to a stratospheric polar vortex strengthening due to a thermal wind response (e.g., Zanchettin et al., 2012; Bittner et al., 2016). Conversely, the local warming from aerosols constrained at higher latitudes decreases the meridional temperature gradient, promoting a

65 weakening of the polar vortex (Kodera, 1994; Perlwitz & Graf, 1995; Stenchikov et al., 2002;

66 Oman et al., 2005; Sjolte et al., 2021). The downward propagation of the stratospheric polar vortex

67 anomaly into the troposphere can lead to regime shifts of the tropospheric Arctic Oscillation and

68 associated anomalous regional surface patterns (e.g., Zanchettin et al., 2012; Zambri et al., 2017).

69 In the case of polar vortex weakening, a critical role is attributed to increased likelihood of sudden

70 stratospheric warming events (SSWs) (Haynes, 2005; Domeisen et al., 2020; Huang et al., 2021;

71 Kolstad et al., 2022, and references therein), whose projection on a negative Arctic Oscillation is

72 expected to bring a series of consequences, including increased frequency of tropospheric

73 blockings and mid-latitude cold air outbreaks (e.g., Ma et al., 2024). However, the negative Arctic

74 Oscillation and associated tropospheric anomalies following SSWs are characterized by a low

75 signal-to-noise ratio (e.g., Charlton-Perez et al. 2018; Zhang et al. 2019). Accordingly, recent

76 studies tend to disagree on this top-down mechanism being a robust dominant feature of climate

77 response to volcanic eruptions (Weierbach et al., 2023; DallaSanta and Polvani, 2023; Kolstad et

78 al., 2022; Azoulay et al., 2021; Polvani et al., 2019; Zanchettin et al., 2022; Toohey et al., 2014).

79 The radiative surface cooling following large volcanic eruptions has been shown to affect the

80 stratospheric polar vortex via a bottom-up mechanism (e.g., Graf et al., 2014; Peings and

81 Magnusdottir, 2015; Omrani et al., 2022). An example of this bottom-up mechanism following HL

82 eruptions is demonstrated in Sjolte et al. (2021) where they linked a weak polar vortex to an

83 increase in wave energy flux from the troposphere into the stratosphere without the meridional

84 stratospheric temperature gradient playing a major role.

85 With this in mind, the importance of transient atmospheric eddies (waves) and eddy-mean flow

86 interactions is becoming increasingly clear in explaining vertical and horizontal propagation of

87 atmospheric perturbations of various origins (e.g. Smith et al., 2022; Nakamura, 2023). DallaSanta

88 et al. (2019) used a hierarchy of simplified atmospheric models to show that eddy feedbacks are

89 crucial in explaining stratosphere-troposphere coupling as well as the stratospheric response alone

90 following a tropical Pinatubo-like eruption. This demonstrates that the anomalous atmospheric

91 circulation response to an enhanced stratospheric sulfate aerosol layer cannot be understood as

92 the mere adjustment to meridional temperature gradients, and that eddy-mean flow interactions

93 and eddy feedback are an essential contribution to such response. Both mechanisms, i.e., the top-

94 down mechanism triggered by local stratospheric heating and the bottom-up mechanism triggered

95 by surface cooling, act together in the real world and in realistic simulations. Therefore, idealized

96   model experiments are required to assess their relative contribution to uncertainty in regional
97   climate variability during the period following the enhancement of the sulfate aerosol layer
98   (Zanchettin et al., 2016).

99   In the definition of a framework to study the climatic effects of a high-latitude enhancement of the
100   stratospheric sulfate aerosol layer, Icelandic volcanism provides for an ideal test bed, as it has
101   played a role in shaping past NH climate variability and will continue doing so. Two Icelandic
102   eruptions during the past 2000 years, namely Eldgjá in ~939 CE and Laki in 1783 CE, are
103   considered to have had a significant impact on climate variability up to the global scale
104   (Brugnatelli and Tibaldi, 2020; Zambri et al., 2019; Oppenheimer et al., 2018; Thordarson and
105   Self, 2003; Stothers, 1998). These types of effusive eruptions are common in Iceland where their
106   duration can extend over years. During part of the eruption time such eruptions can become
107   explosive (referred to as mixed-phase eruptions) when ascending magma in a conduit comes in
108   contact with water as was considered the case with both Eldgjá and Laki, explaining their
109   widespread impacts. Eruption history as well as dense monitoring network of Icelandic volcanic
110   systems tell us that many of these systems are currently on the verge of an eruption, having already
111   produced some of the largest volcanic eruptions over the past millennia (e.g., Öræfajökull,
112   Bárðabunga and Hekla, Larsen & Guðmundsson, 2014; Barsotti et al., 2018; Einarsson, 2019).
113   Therefore history and current activity makes these types of eruptions an ideal reference case to
114   explore the potential climatic impacts of high-latitude enhancements of the stratospheric sulfate
115   aerosol layer and to test hypotheses about the underlying mechanisms driving the climate
116   response. This is the focal point of this study where we investigate for the first time the role of
117   wave-mean flow interactions and SSWs in the atmospheric circulation response to a HL volcanic
118   eruption. For this we perform idealized, long-lasting HL volcanic perturbation experiments using
119   the Community Earth System Model version 1 (CESM1) in its coupled and atmosphere-
120   standalone configurations. We evaluate the NH response during the first three winters following
121   the eruption, referred to as post-eruption winters in the text, and assess the dominating
122   mechanism in each winter. This paper is organized as follows: Section 2 describes the model,
123   experimental design and diagnostics; results are presented in section 3 followed by discussions in
124   section 4 where we end with concluding our results in section 5.

125

126

2 Methods

2.1. Numerical Model

We use the Community Earth System Model (CESM) version 1, developed by the National Center for Atmospheric Research (NCAR). In our configuration of CESM1, the atmospheric component is the Whole Atmosphere Community Climate Model, version 4 (WACCM4, Marsh et al. 2013). WACCM4 includes 66 vertical levels (up to $5.1 \times 10{-}6$ hPa, ~140 km) and uses CAM4 physics. We use the specified chemistry version of WACCM4 (SC-WACCM4), which is computationally less expensive to run, but simulates dynamical stratosphere-troposphere coupling and stratospheric variability like SSWs and the polar vortex with skills comparable to the interactive chemistry model version (Smith et al., 2014). CESM1/WACCM4 uses the Community Atmospheric Model Radiative Transfer (CAMRT) to parameterize the radiative forcing where it has been shown to accurately represent stratospheric aerosols by f. ex. simulating the temperature response following Mt. Pinatubo in 1991 (Neely et al., 2016). The SC-WACCM4 experiments are run with a horizontal resolution of 1.9° latitude by 2.5° longitude and include present-day (year 2000) radiative forcing. A repeating 28-month full cycle of the Quasi-biennial Oscillation (QBO) is included in the SC-WACCM4 experiments through nudging of the equatorial stratospheric winds to observed radiosonde data. In the coupled ocean-atmosphere configuration, the ocean component of CESM1 is the Parallel Ocean Program version 2 (POP2). CESM1 also includes the Los Alamos sea-ice model (CICE), the Community Land Model version 4 (CLM4) and the River Transport Model (RTM). CLM is run at a horizontal resolution of 1.9°x2.5°, POP2 and CICE are run at nominal 1° resolution with higher resolution near the equator than at the poles. Further details about CESM1 are given in Hurrell et al. (2013).

2.2. Volcanic Forcing File

We use the Easy Volcanic Aerosol (EVA) forcing generator (Toohey et al., 2016). EVA provides zonally symmetric stratospheric aerosol optical properties as a function of time, latitude, height, and wavelength (see detailed information on the tool in Toohey et al., 2016). EVA has been used to generate volcanic forcing in both idealized volcanic experiments (e.g., Zanchettin et al., 2016) and realistic paleoclimate simulations (Jungclaus et al., 2017) contributing to the sixth phase of the coupled model intercomparison project.

157   We use EVA to prescribe the volcanic aerosol loading corresponding to that of the 1991 Mt.

158   Pinatubo eruption (14.04 Tg SO_2), but at 45° N. Since the model reads the volcanic forcing as

159   aerosol mass (kg/kg), we scale our forcing file by using the standard aerosol mass input file for

160   CAM4 and 5 (see Neely et al., 2016, Table 1) for the same eruption. A monthly scaling factor was

161   derived from this linear relationship between the aerosol extinction ($1/m^2$) and the aerosol mass

162   (kg/kg) that was used to scale the raw EVA forcing data (Fig. 1). From these scaled forcing data,

163   the aerosol optical properties for our experiments are obtained with a two-step approach. First, we

164   move the injection location northwards so that the center of the aerosol mass is at 65° N latitude

165   and spans 10-28 km in altitude. Then, we define the start of the eruption to be May 1st and prolong

166   the peak of the forcing by extending in time the highest monthly value in the so-obtained forcing

167   data, so that the decline in aerosol mass begins 6 months after the start of the eruption or on

168   November 1 (see Fig. 1). We thus obtain aerosol optical properties for an idealized, long-lasting

169   high-latitude NH eruption. In this experiment we assume stratospheric injection only, although

170   similar eruptions in the natural world would likely inject part of the total aerosol mass within the

171   troposphere during the eruption. Past NH eruptions like Eldgjá and Laki had an atmospheric SO_2

172   loading of 219Tg and 122Tg respectively that was carried aloft with the eruptive column up into

173   the upper troposphere with portions of the aerosols reaching the lower stratosphere during the

174   eruptions (Thordarson et al., 2001). Hence our experiment can also be considered as a 6-month

175   stratospheric aerosol injection that is analogous to similar although smaller eruptions (as compared

176   to Laki) without the tropospheric aerosols.
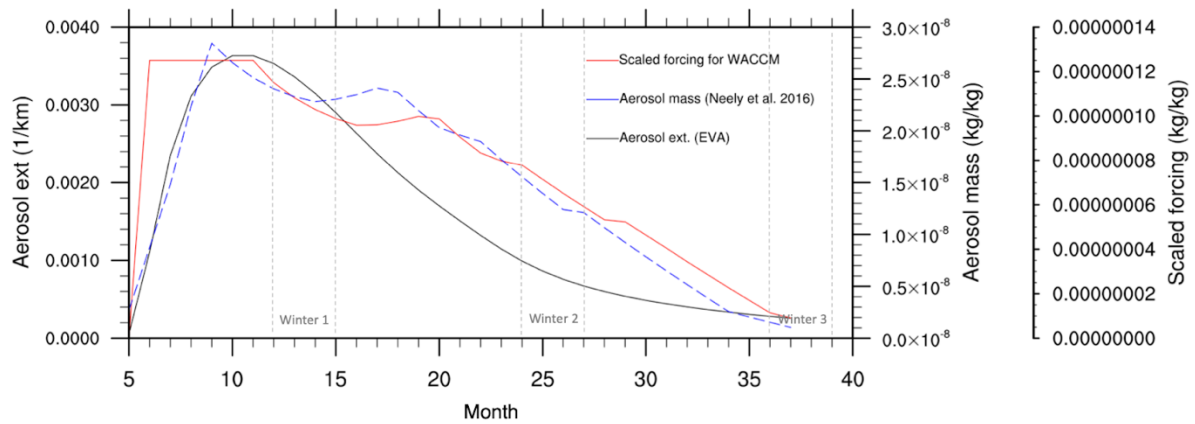
177

178

179

180

Figure 1: The time series of the original EVA aerosol extinction output (1/km, black curve) and the aerosol mass of the volcanic forcing file of Neely et al. (2016) (kg/kg, blue dashed curve) used for deriving the linear scaling coefficient for the conversion of EVA output into WACCM4 input (kg/kg, red curve). The horizontal axis is time (months) from the start of the eruption. Here we assume that the aerosol lifetime at 65° N is the same as at 45° N. Dashed vertical lines show the three winters that we focus on in this study.

2.3. Experimental design

We ran two volcanic perturbation experiments with CESM1. The first experiment is conducted with the atmosphere-only version of the model, where boundaries to SC-WACCM4 are provided by prescribed fields of sea-surface temperature (SST) and sea-ice concentration (SIC) corresponding to the 1979-2008 monthly climatology of HadISST observations (Rayner et al., 2003). We refer to this experiment as *atm-only*. The second experiment is conducted with the coupled version of the model, henceforth referred to as *cpl*. For each experiment we run 20 ensemble members including the volcanic forcing and 20 paired ensemble members without the volcanic forcing and otherwise identical to the volcanic simulations, which we refer to as the control.

The atmosphere-only experiments were run over three full years, which provides two full winters after the onset of the eruption. We found that there was no need to extend the simulations further given the duration of the forcing and short memory of the atmosphere. The coupled experiments follow a similar protocol but they were integrated over 15 years to assess the response influenced by oceanic dynamical adjustment. However, in this study we only focus on the first three winters following the eruption. We define the first post-volcanic winter as December of the starting year (year 0) and the following January and February (year 1), the second post-volcanic winter is then December of year 1 and the following January and February of year 2 etc.

Because the QBO is prescribed, and given its importance for the atmospheric circulation and the distribution of volcanic aerosols within the stratosphere (Thomas et al., 2009; DallaSanta et al., 2021; Brown et al., 2023), we have been careful in homogeneously sampling the QBO phasing that is imposed on the 20 ensemble members. For this, we shift the 28-month QBO cycle by one month for every ensemble member, so that the phasing of the QBO differs from one ensemble

211 member to the next (Elsbury et al., 2021). This avoids potential biases in the climatic response that
212 may be induced by any dominating QBO phase.

213

214 **2.4. Diagnostics**

215 Model output is analyzed by computing paired anomalies, defined as deviations of each volcanic

216 simulation from the corresponding control simulation (Zanchettin et al., 2022) (volcanic minus

217 control). The statistical significance of the ensemble mean of paired anomalies is assessed at the

218 95% confidence interval, calculated from all 20 ensemble members, using a two-sided Student's t-

219 test in addition to a Kolmogorov-Smirnov test.

220 To evaluate the effects of planetary waves on the zonally-averaged stratospheric response, we use

221 the Eliassen Palm (EP) flux and its divergence (Edmon et al., 1980) in addition to the 3D

222 generalization of the EP flux, the Plumb flux (Plumb, 1985), for a longitudinal representation in

223 the lower troposphere and stratosphere. We identify SSW events by using an algorithm following

224 the procedures described in Charlton and Polvani (2007), where mid-winter sudden warming

225 events are determined to take place if the 10 hPa zonal-mean zonal wind at 60°N becomes easterly.

226 Once a warming is identified, no day within 20 days of a central date, defined as the first day in

227 which the daily mean zonal-mean wind at 60N and 10hPa is easterly, can be defined as an SSW.

228 Changes in conditions for large-scale planetary waves propagation (waveguides) are examined

229 using the optimal propagation diagnostic for stationary planetary waves, described in Karami et

230 al. (2016). This metric is based on the construction of PDFs for positive values of the refractive

231 index (Matsuno 1970), as a function of zonal and meridional wave numbers. The refractive index

232 is calculated using daily zonal wind and temperature at all levels, to derive monthly and zonally-

233 averaged probabilities for stationary Rossby waves to propagate through the atmosphere, in

234 function of latitude and pressure level. This is calculated for zonal wave numbers k=1,2,3 and

235 meridional wave numbers l=1,2,3 (large-scale waves), and we average the probabilistic refractive

236 index for each of the nine combinations of k and l, to provide a general estimate of chances for

237 propagation of stationary planetary waves. For the eddy feedback calculations we compute the

238 square of the local correlation across the ensemble members between DJF zonal-mean zonal wind

239 and the divergence of the northward EP flux (delta phi F phi) averaged over 600-200 hPa (Smith

240 et al. 2022). In addition, we compute the rate of temperature (K) changes in the 2m temperature

241 (T2m) gradient using spherical harmonics to yield a T2m gradient in the meridional (dZ/dlat) and
242 zonal (dZ/dlon) directions.
243
244 **3 Results**
245 In the following sections we will investigate the *cpl* experiment to characterize the forced response
246 and identify the mechanism by utilizing the information provided by the *atm-only* experiment. We
247 begin our investigation in the upper atmosphere before making our way towards the surface.
248
249 **3.1. Volcanic radiative forcing**
250 The net shortwave (SW) and longwave (LW) downward flux at the top of the atmosphere show an
251 expected behavior following a stratospheric sulfate injection where we see a decrease in the SW
252 due to scattering and an increase in the LW due to absorption around the injection location (Fig.
253 2c-f). Temporal perturbations of SW fluxes for both *cpl* and *atm-only* are influenced by the obvious
254 strong seasonal evolution in solar insolation, where we see strong anomalies during the first
255 summer north of 30° N than then becomes more confined to the mid latitudes as winter progresses
256 with a slow decrease towards the end of the third year (Fig. 2c-d).
257 LW anomalies also show seasonal evolution with stronger LW flux at mid latitudes compared to
258 at high latitudes during summer that continues into the winter season and remains significant
259 throughout most of these three years. During winter, the LW anomalies are present at high latitudes
260 where the SW anomalies are absent. The latitudinal bands of radiative flux anomalies correspond
261 to the maximum values of the aerosol mass between 60 and 70° N, and the aerosol mass being
262 largely confined north of 45° N (Fig. 2a-b). Overall, the radiative forcing is largely bounded by
263 the NH extratropics with the exception of a slight significant increase around 30-60° S in the
264 second and third summer (Fig. 2c-d) that is visible at around 14-15 km a.s. (Fig. 2b). This occurs
265 due to spatial features in the Neely et al. (2016) aerosol forcing that we use for scaling, where a
266 slight aerosol increase occurs at lower latitudes, although this is not detectable when the aerosol
267 mass is averaged through the atmospheric column with respect to time (Fig. 2a). We also detect a
268 slight difference in the LW and SW fluxes that arises from differences in high cloud cover between
269 *atm-only* and *cpl*, where *cpl* shows a decrease in high cloud cover in the northern high-latitudes,
270 compared to *atm-only* (not shown).
271
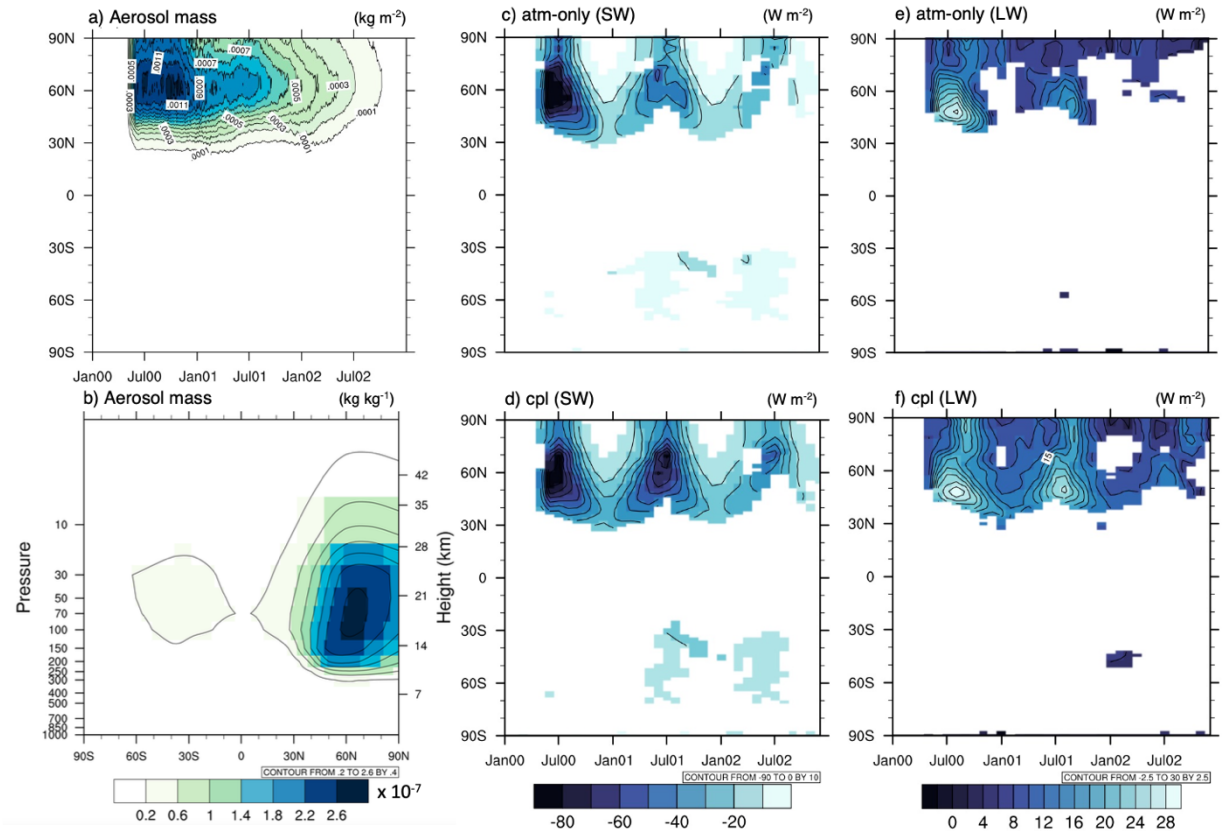
Figure 2: Left panels: a) Average aerosol column mass time evolution in kg/m2 and b) pressure vs. latitude slice of the aerosol mass in kg/kg (3-year average). Aerosol mass is the same in cpl and atm-only. c) and d) show the time evolution of the net SW flux (downward) anomaly at the top of the atmosphere, and e) and f) the same but for net LW flux anomaly, resulting from the volcanic aerosol mass, in c) *atm-only* and d) *cpl* where coloured areas indicate 99% significance compared to the control experiment according to a Student's t-test.

3.2. Stratospheric response

The strong seasonality in the LW perturbations described above also characterizes stratospheric temperatures, where a strong increase in the zonally averaged temperature at 50 hPa (T50) is detected north of 30° N during post-eruption summers in both experiments (Fig. 3a and 3b). This summer warming is followed by a net cooling of the polar stratosphere in the first winter seen for both *cpl* and *atm-only*. A clear difference in the T50 response in the two experiments is seen in

winter 2, where *cpl* yields warming over polar latitudes while *atm-only* yields cooling (Fig. 3a,b). This reveals the intra-seasonal dynamical effects in the *cpl* experiment beyond the direct radiative response as we will see later on. The contrasting temperature response is accompanied by an opposite response in the zonal-mean zonal winds at 10hPa (U10) between 70 and 80° N. This U10 response is an indicator of the state of the polar vortex, where a polar vortex weakening is detected in winter 2 for *cpl* but a strengthening *atm-only* (Fig. 3c-d). Figures 3c-d do show a large ensemble spread in the zonal mean U10 winter response that is evident of a low signal to noise ratio. While the first winter in *cpl* and the first two in *atm-only* show little statistical significance according to a Kolmogorov-Smirnov test, this significance does increase for winter 2 in the *cpl* experiment. We also see this weakening in the zonal mean U50, also showing stronger significance during winter, (Supplementary Fig. S3) but not as clearly as in the zonal mean U10. However, for consistency we will mainly be focusing on the U50 response in the following section where this response is clear over the NH polar cap. The difference between *cpl* and *atm-only* will be in the focus in the following sections.

b) T50 (atm-only)

CONTOUR FROM -10 TO 12 BY 2

°C

305

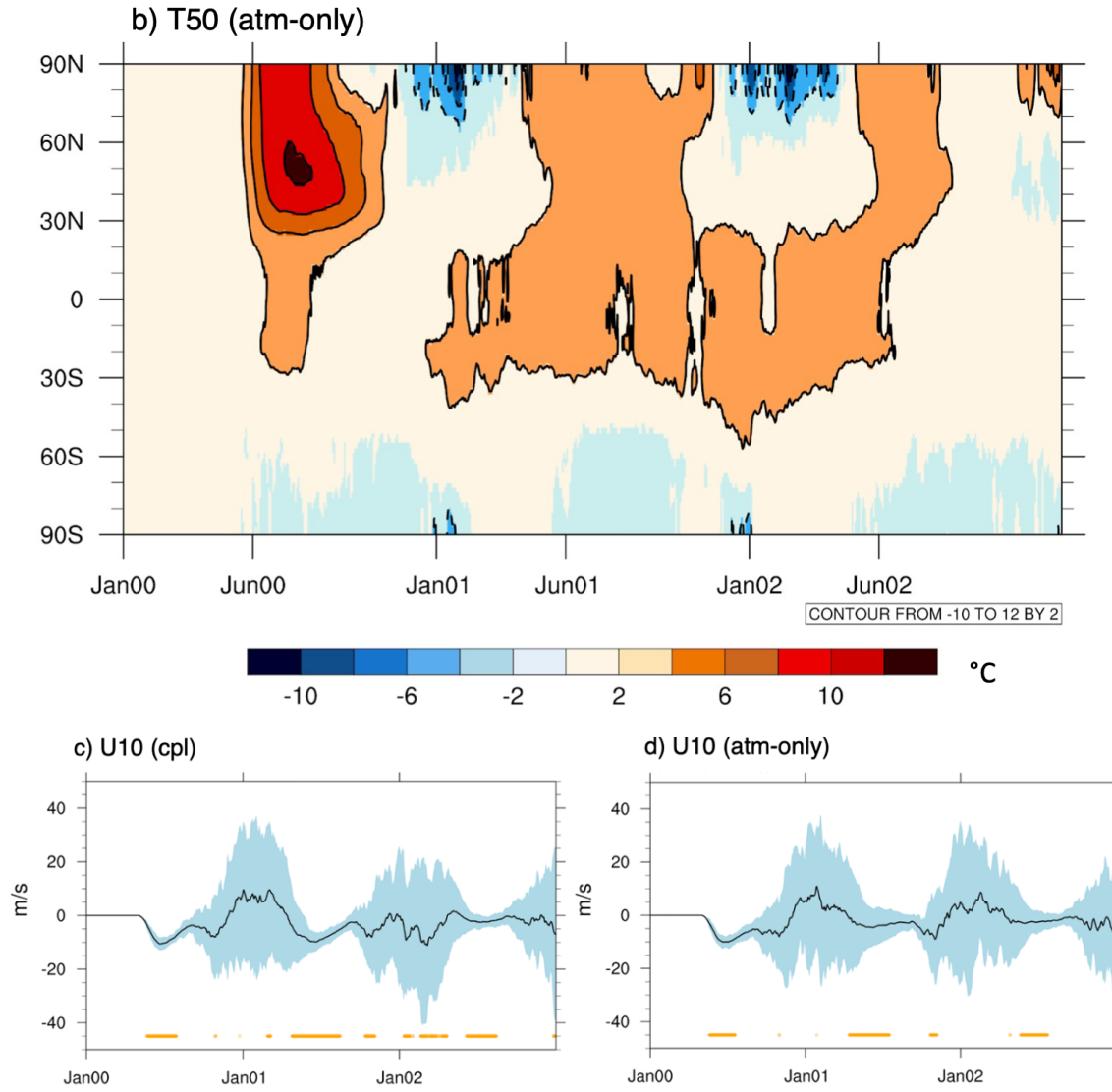c) U10 (cpl)

d) U10 (atm-only)

306
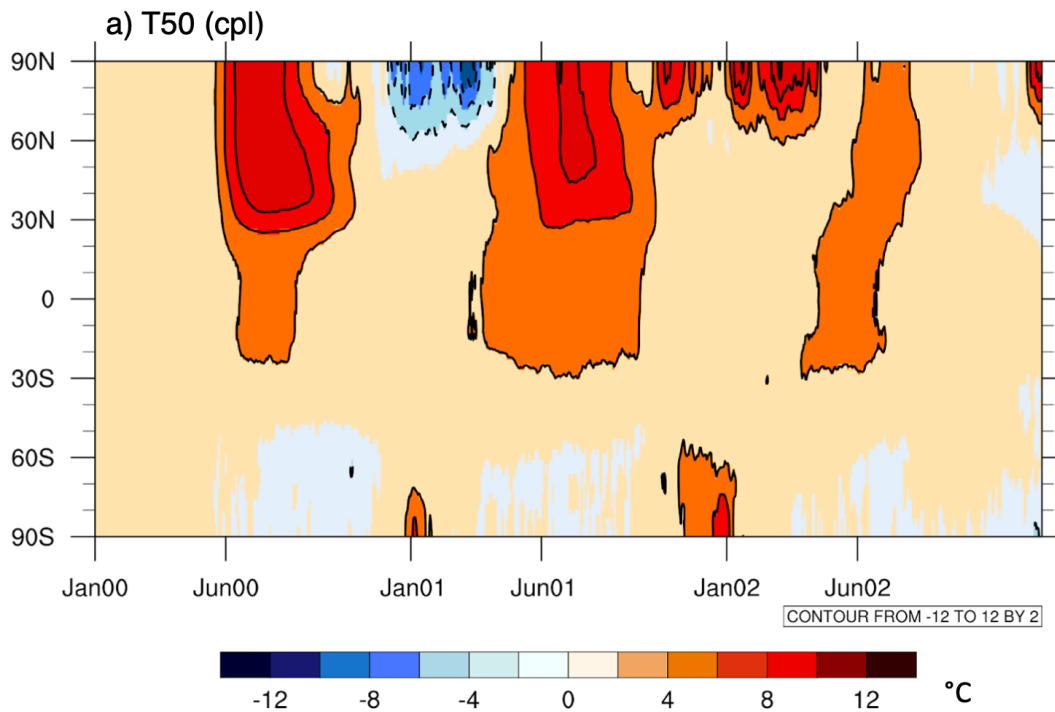
Figure 3. a,b) Latitude versus time response of T50 anomalies in a) *cpl* and b) *atm-only*. Contours are significant in 95% confidence intervals according to a student's t-test. c,d) Stratospheric polar vortex response shown as the zonal mean U10 anomalies between 70 and 80° N for c) *cpl* and d) *atm-only*. Black lines show the ensemble mean anomalies and blue shadings show the ensemble +/- 2 standard deviation anomaly range. Orange markers indicate when the difference between perturbed and unperturbed experiments becomes significant (p<0.05) according to a Kolmogorov-Smirnov test.

307
308
309
310
311
312
313
314
315
316

12

3.2.1 - First post-eruption winter

In the *cpl* experiment, the polar vortex strengthening in winter 1 is associated with extensive anomalies in temperature and zonal wind at 50 hPa (Fig. 4a). The anomalous temperature pattern consists of cooling at high latitudes and into the midlatitudes over the Atlantic, and warming over large swaths of the subtropics (to 20° N) and into the midlatitudes over the Pacific. This temperature pattern is also identified in the zonal mean T50 (Fig. 3b). Similarly, the zonal wind weakens into the midlatitudes over the Pacific while it is stronger in mid to high latitudes over the Atlantic. The strong upward EP flux (black arrows) is an indicator of the direction of propagated waves originating at the surface around the midlatitudes, where the horizontal and vertical EP flux components are proportional to the eddy momentum and heat flux, respectively (Fig. 4d). A convergence (negative divergence, dashed red contours) in the EP flux is detected in the upper troposphere that acts to weaken the tropospheric westerlies (Fig. 4d and Fig. S2). However, the EP flux and its convergence within the stratosphere does not appear to impact the stratospheric mean flow and the polar vortex. Therefore the local heating due to the volcanic aerosols and the associated increase in the meridional temperature gradient in the stratosphere appear to dominate the response of the polar vortex via thermal wind response, also depicted by the LW anomalies (Fig. 2f). Winter 1 in *atm-only* shows a similar thermal wind mechanism at play in the stratosphere as for the *cpl* experiment (Fig. 5a and 4a, respectively). In that case, less obvious tropospheric influences are detected, due to lack of forced surface cooling, as seen in the limited anomalous upward wave activity detected by the EP flux diagnostics (Fig. 5c).
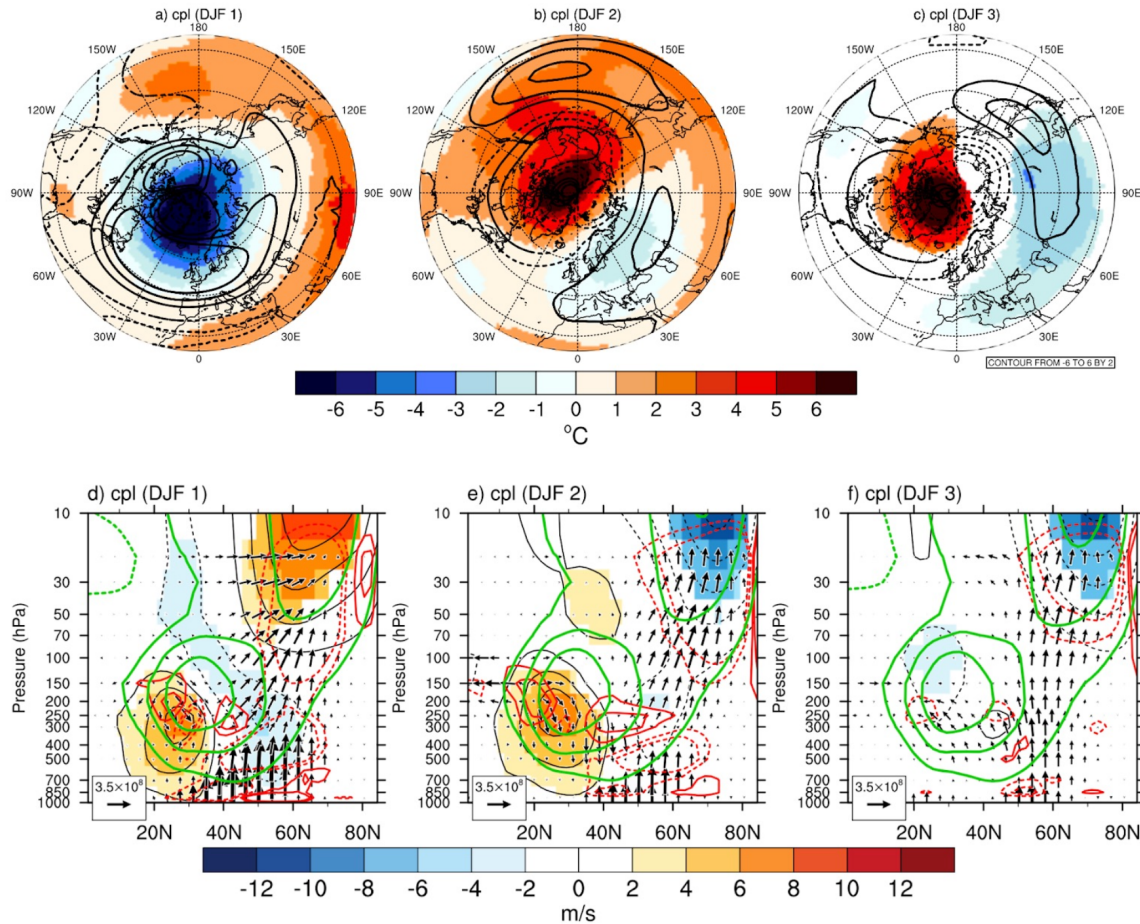
Figure 4: Winter stratospheric response in the *cpl* experiment. a-c) U50 (contours) and T50 (shading: red = warming, blue = cooling) response for winters 1-3, respectively. d-f) EP flux (arrows) and divergence (red contours) response, along with zonal-mean zonal wind response (black contours and shading: red = strengthening, blue = weakening) and climatology (green contours) in winters 1-3, respectively. Contours and color-shaded areas indicate 95% significance according to a Student's t-test. Only vectors that are significant at the 95% confidence interval are shown.
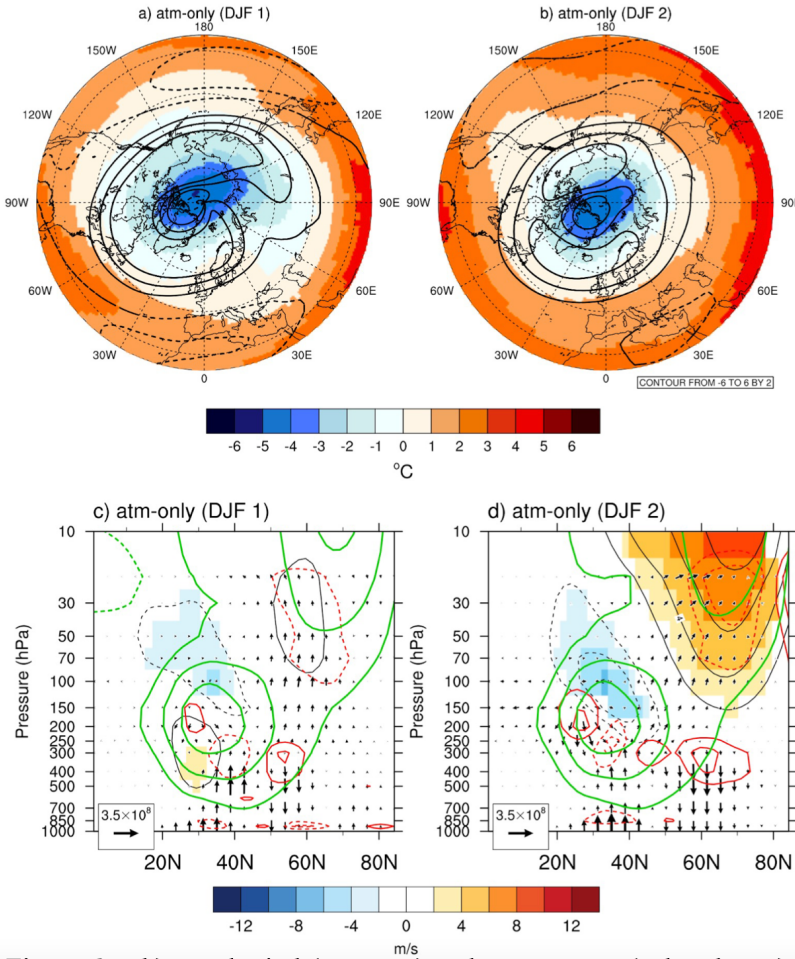
Figure 5: The same as Fig. 4 but for the *atm-only* experiment. a-b) Zonal wind (contours) and temperature (shading) response at 50 hPa for winter 1 and winter 2, respectively. c-d) EP flux (arrows) and divergence (red contours) response along with zonal-mean zonal wind (black contours) and pure climatology (green contours, 2m) in winters 1-2, respectively. Contours and colored area indicate 95% significance according to a Student's t-test.

3.2.2. Second post-eruption winter

A stark difference in the polar vortex response is detected between *cpl* and *atm-only* in winter 2. While *atm-only* exhibits a response similar to winter 1 (Fig. 5b), a significant warming over North America and the North Pacific emerges in *cpl* along with a weakening of U50 at high latitudes (Fig. 4b) indicating a shift of the polar vortex towards Eurasia. This warming at high latitudes then coincides with a slight LW absorption at high latitudes (Fig. 2f). The U50 weakening is not uniform throughout the longitudes explaining the lack of response detected in the zonal mean U50 (Fig.

363 S3), where one needs to go to U10 to get a clear response in the zonal-mean zonal wind (Fig. 3c).

364 An anomalously strong upward propagation of planetary waves persists in the *cpl* (Fig. 4e), with

365 a stronger upward EP flux now protruding into the stratosphere above 20hPa in contrast to winter

366 1. The upward EP flux and its convergence in the polar stratosphere are evident of their

367 contribution towards the weakening of the U50 and a general dominance over the effects of thermal

368 forcing by aerosols that have been, at this stage, substantially reduced (Fig. 1).

369 Similar wave propagation pattern as identified in the *cpl* experiment is known to be associated

370 with SSWs. We suspect that the decrease in the T50 difference between mid- and high latitudes

371 can act as a trigger for a weaker polar vortex in addition to the stratosphere absorbing the upward

372 propagating waves that is known to cause warming over the polar cap (Kodera et al., 2016;

373 Kretschmer et al., 2018). We will see further evidence of this in the next section.

374

375 **3.2.3. Third post-eruption winter**

376 The results in this section only refer to the *cpl* experiment since winter 3 is lacking in *atm-only*.

377 The SSW-like pattern of winter 2 clearly continues into winter 3, where most of the volcanic

378 aerosols have decreased to the extent that their radiative impacts no longer dominate. An exception

379 is the confinement of T50 warming over the polar stratosphere (Fig. 4c). Furthermore, anomalous

380 upward propagation of planetary waves continues to persist (Fig. 4f). This upward wave flux in

381 addition to the T50 warming resembles a pattern that behaves much like absorbing SSWs defined

382 by Kodera et al. (2016). To examine this response further we define SSWs based on the reversal

383 of the zonal-mean zonal winds at 60° N and at 10hPa between November and March according to

384 the method of Charlton and Polvani (2007) .

385

386 Results from the SSW analysis are presented in Fig. 6. No significant increase in SSWs is found

387 in winter 2, despite the SSW-like pattern detected. This changes in winter 3 when the difference

388 between perturbed and unperturbed experiment becomes statistically significant, with 27 SSWs

389 occurring in our forced experiment compared to only 6 in the control experiment. This increase in

390 SSWs agrees well with the U50 and T50 anomalies of winter 3 (Fig. 4c). During winter 2, the

391 warming of the polar stratosphere is as strong as in winter 3 but more spread out into midlatitudes.

392 These results are also in agreement with the stratospheric Plumb flux in winter 3 (Fig. S1c) where

393   the upward flux is mostly circumpolar between 40° and 60° N, showing further evidence of the

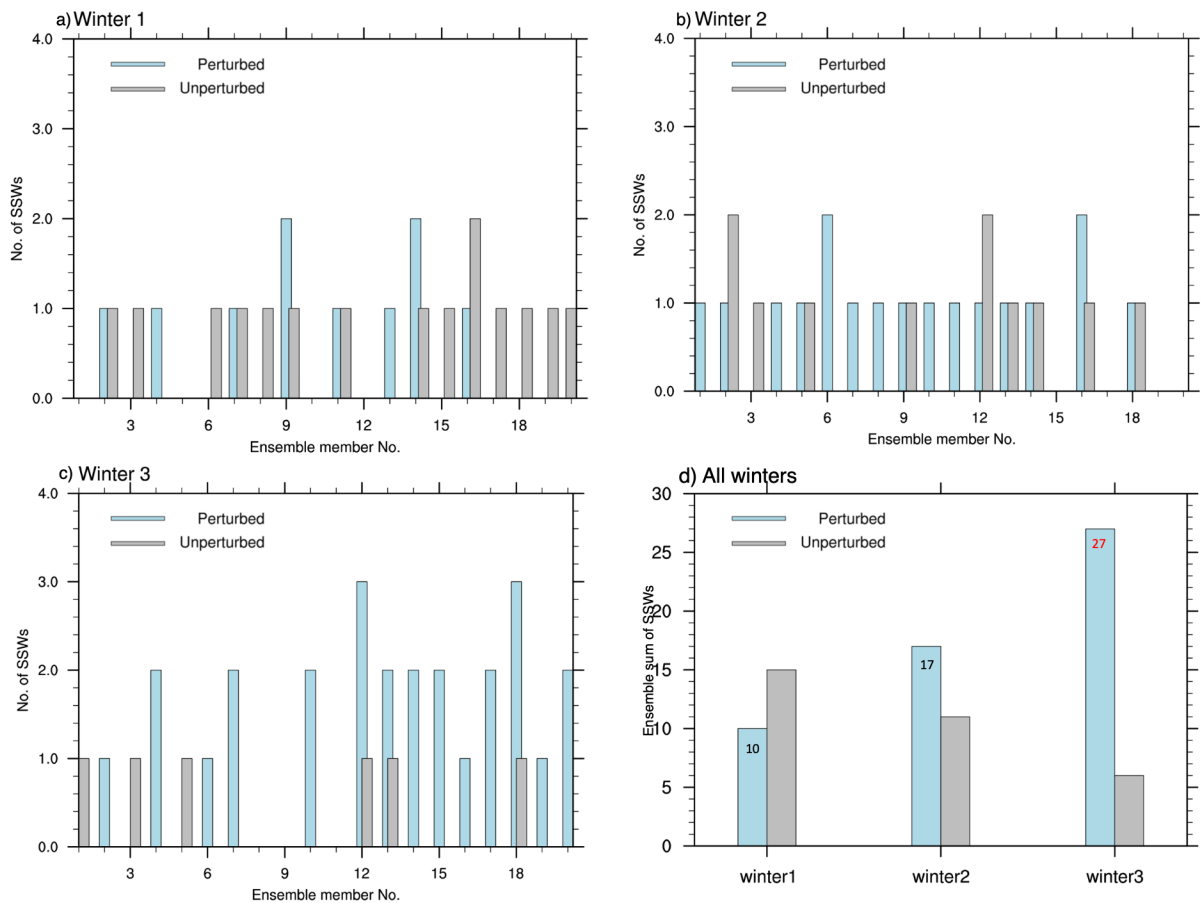394   SSWs detected.

395

396

397   Figure 6: a-c) The number of SSWs during winters 1-3 for each ensemble member in the *cpl*

398   experiment and d) The sum of all SSWs in each experiment for all 20 ensemble members of winters

399   1-3 both for *cpl* (light-blue bars) and control (gray bars). The color red indicates 95% significance

400   according to a two-sided Student's t test.

401

402   When comparing the ensemble sum of SSWs in the perturbed and unperturbed experiment using

403   a Kolmogorov-Smirnov test (Fig. 5d), a significant increase in the number of SSWs occurs in

404   winter 3 (p=0.0135). This underlines the generally strong SSW response occurring in winter 3,

405   when the fraction of ensemble members having more than 1 SSW per winter increases to 50% (10

406   ensemble members) in winter 3 compared to only 10% in winters 1-2. Of these 10 ensemble

407   members, two members show three SSWs per winter that can be considered highly unlikely based

17

408 on historical records. Although winters with more than 1 SSWs are considered unusual, examples

409 do exist in the observational record of multiple SSWs in one winter, like the winter of 1998/1999

410 and 2009/2010 (Kodera et al., 2016 and Ineson et al., 2023 respectively).

411 To better understand the cpl SSWs response, we also did an SSW analysis on *atm-only* (Fig. S7)

412 where 50-75% less SSWs were detected in the perturbed simulation compared to the unperturbed

413 one. Such a response should not be unexpected during the forced polar vortex strengthening as

414 detected in *atm-only* (see Fig. 5). Furthermore, only single SSWs per winter were detected in all

415 20 ensemble members of the perturbed simulation while two (one) ensemble member(s) detected

416 double SSWs per winter 1 (winter 2) in the unperturbed simulation. Although these results do show

417 strong evidence of an increase in the number of SSWs in the *cpl* simulation, internal variability is

418 large and the frequency of SSWs fluctuates substantially between the three winters in the

419 unperturbed simulation.

420 Since this is indicative of a low signal-to-noise ratio and uncertainties in the response of polar

421 vortex variability, we tested the potential impact of ensemble size on the signal-to-noise ratio for

422 two key diagnostics of our mechanism, namely U10 and SSW. We express the signal-to-noise ratio

423 as the uncertainty related to the expected (i.e., ensemble mean) response, calculated as standard

424 error of the mean of post-eruption paired anomalies for the first three post-eruption winters. The

425 standard errors converge toward the value obtained for the full 20-member ensemble for all winters

426 and both variables (Figure 7), with a common tendency of growing uncertainty in the expected

427 response with the ensemble size. The mean curves consistently level off for ensemble sizes larger

428 than 10, suggesting that the full ensemble estimate is representative of uncertainty in the expected

429 response for larger ensemble sizes. Otherwise, winter 3 produces larger uncertainty than winters 1

430 and 2, suggesting a less constrained forced response. This is especially evident for estimates of

431 standard error of SSW anomalies and ensemble sizes larger than 15, where winters 1 and 2 closely

432 superpose on each other while winter 3 does not overlap with winters 1 and 2 within the 5-95th

433 percentile range. Overall, the flattening of the ensemble-mean expectations on the standard error,

434 and the large values diagnosed in winter 3, suggest that the winter 3 response features an

435 intrinsically lower signal-to-noise ratio. In fact, since the value of full-ensemble mean SSW paired

436 anomaly in winter 3 (+1.05 events) is similar to the associated expected standard error (+1.02

437 events) we conclude that even a much larger ensemble would not provide more certainty in the
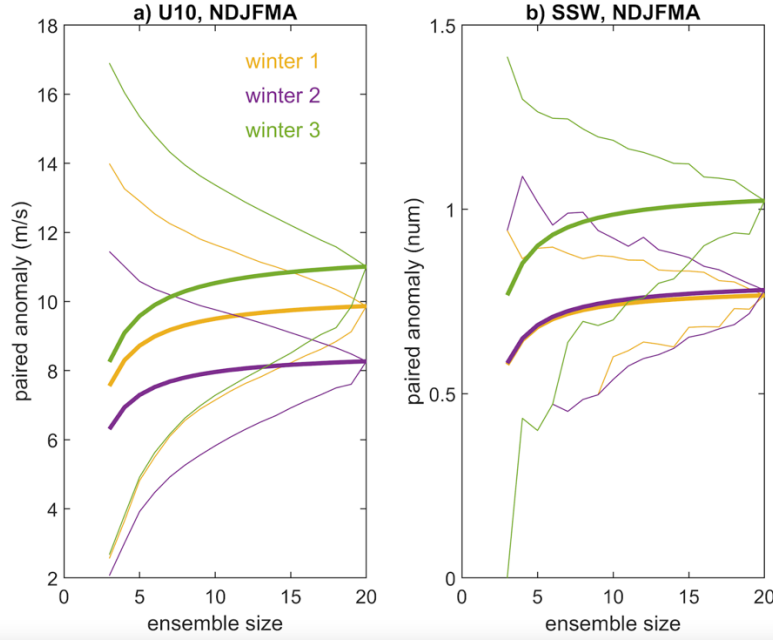
438 signal detected.

Figure 7: Impacts of ensemble size and spread on the volcanic signal. Ensemble mean (thick lines) and associated standard errors (thin lines, 5-95 percentile range) of paired anomalies calculated for different ensemble sizes and for the first three post-eruption extended winter seasons (November to April) for stratospheric zonal-mean zonal wind (a) and number of sudden stratospheric warming events (b). For each ensemble size from 3 to 20, the mean and the standard error of the mean are calculated for all sub-ensembles determined by all possible permutations of the full ensemble for the considered size. Then, means and 5th and 95th percentiles of the so-obtained standard errors for each ensemble size are plotted.

According to the above, the evolution in *cpl* from winter 1 to winter 3 can be summarized as follows: In the first winter, the thermal forcing appears to be stronger than the upward wave flux because of the large amount of aerosols present, thereby dominating the response that causes the polar vortex strengthening and the inclusion of cold polar air within. In the second winter, the thermal forcing from the volcanic aerosols at midlatitudes has decreased where it is now mostly confined to higher latitudes as seen both in the LW flux and T50 (Fig. 2f and Fig. 3b). We suspect that in addition to the aerosol decrease, this slight decrease in the temperature difference between high and midlatitudes allows the strong upward wave flux to dominate and enter the upper stratosphere. There in the stratosphere, the waves are absorbed that causes further warming over the polar cap in addition to weakening the zonal stratospheric winds (Fig. 5b and Fig. 4b). This

459   upward wave flux and weaker winds continue into the third winter, where winter 2 likely acts as a

460   precursor, allowing for SSWs to develop more frequently as detected in the T50 warming that is

461   now confined over the polar cap (Fig. 4c and Fig. 5c, respectively). The expected absence of a

462   surface response is obvious in our *atm-only* experiment where basic physical mechanism, via the

463   thermal wind balance due to radiative heating, dominates the atmospheric circulation response in

464   the first two post-eruption winters, with a strong stratospheric polar vortex isolating the cold air

465   over the polar regions in the second winter as in the *cpl* experiment (Fig. 5a-b).

466

467   **3.3. Tropospheric response**

468   What is it then that drives this polar vortex weakening and the SSW response in the *cpl* experiment?

469   To examine in more detail the origin of the upward wave fluxes in winters 2 and 3 of the *cpl*

470   experiment that causes the detected polar vortex weakening and the SSWs, we now turn our

471   attention towards the troposphere.

472

473   We begin by comparing the response of T2m, vertical Plumb flux at 850 hPa and 200 hPa zonal

474   wind, in *cpl* (Fig. 8) and in *atm-only* (Fig. 9).

475   As a response to the decrease in SW flux following the eruption, extensive and heterogeneous

476   cooling is identified in the T2m anomalies in winters 1-3 (*1-2 for atm-only*) over latitude bands

477   that contain the most significant SW flux decrease (Fig. 2d, Fig. 8a-c and Fig. 9a-b). The strongest

478   cooling occurs over northeastern North America and along the Asian midlatitudes in winter 1, with

479   much larger amplitude in *cpl* than in *atm-only* (Fig. 8a versus Fig. 9a). In *cpl*, the SST significantly

480   cools down (Fig. S5), which extends the area of negative T2m anomalies over the ocean, in

481   particular over the northwestern North Pacific in winter 1 (Fig. 8a). There it progresses from an

482   initial preferential surface cooling over the midlatitudes in winter 1 to a later cooling of polar

483   regions in winter 3 (Fig. 8c). In *atm-only*, the surface response is hampered over the ocean by the

484   experimental design, and T2m anomalies are therefore confined to landmasses, yielding an overall

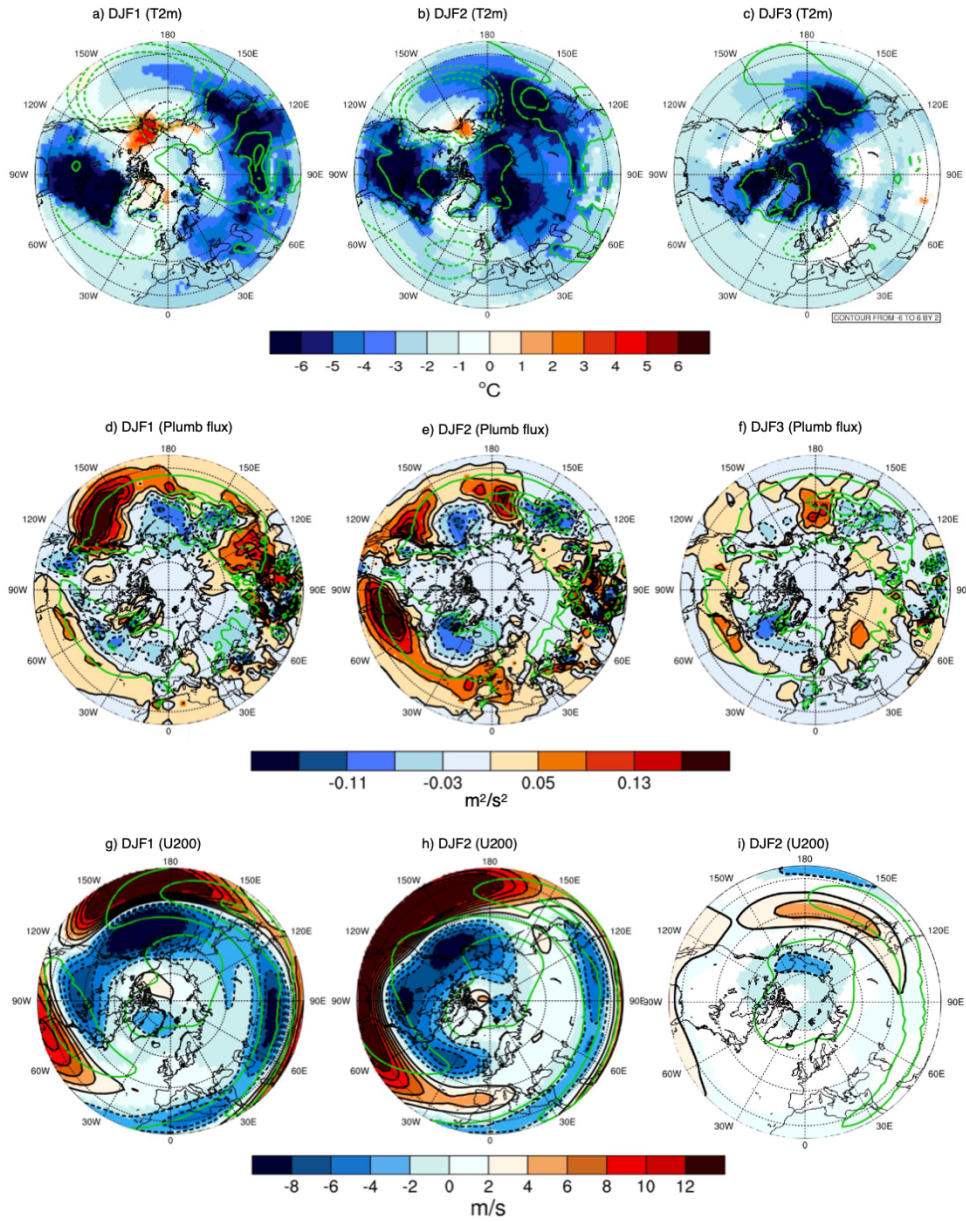485   much weaker temperature response compared to *cpl* (Fig. 9a-b).

486

487

488

Figure 8. a) Response of 2-meter air temperature (°C) in *cpl* (color), and sea-level pressure (green contours), for winter 1. b) Same as *a)* but for winter 2. c) Same as *a)* but for winter 3. d) Response of 850 hPa vertical component of the Plumb flux (m^2/s^2) in *cpl*, and the climatology as green contours from -8 to 12 by 2, for winter 1. e) Same as *d)* but for winter 2. f) Same as *d)* but for winter 3. g) Response of 200 hPa zonal wind (m/s) in *cpl*, and the climatology as green contours from -0.15 to 0.15 by 0.04, for winter 1. h) Same as *g)* but for winter 2. i) Same as *g)* but for winter 3. Contours and colored areas indicate significance at the 95% confidence interval according to a Student's t-test.
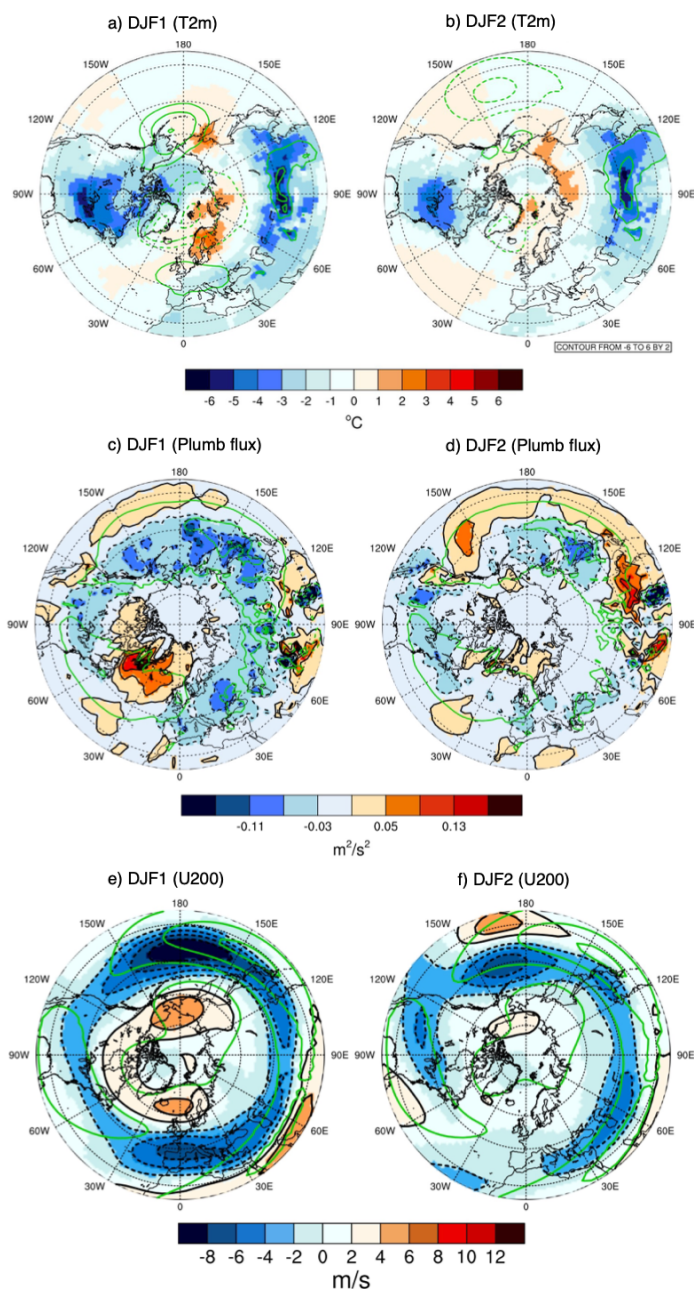
Figure 9. a) Response of 2-meter air temperature (°C) in *atm-only,* and sea-level pressure (green contours), for winter 1. b) Same as *a)* but for winter 2. c) Response of 850 hPa vertical component of the Plumb flux (m²/s²) in *atm-only*, and the climatology as green contours from -8 to 12 by 2, for winter 1. d) Same as *c)* but for winter 2. e) Response of 200 hPa zonal wind (m/s) in *atm-only*, and the climatology as green contours from -0.15 to 0.15 by 0.04, for winter 1. f) Same as *e)* but for winter 2. Contours and shaded areas indicate significance at the 95% confidence interval according to a Student's t-test.
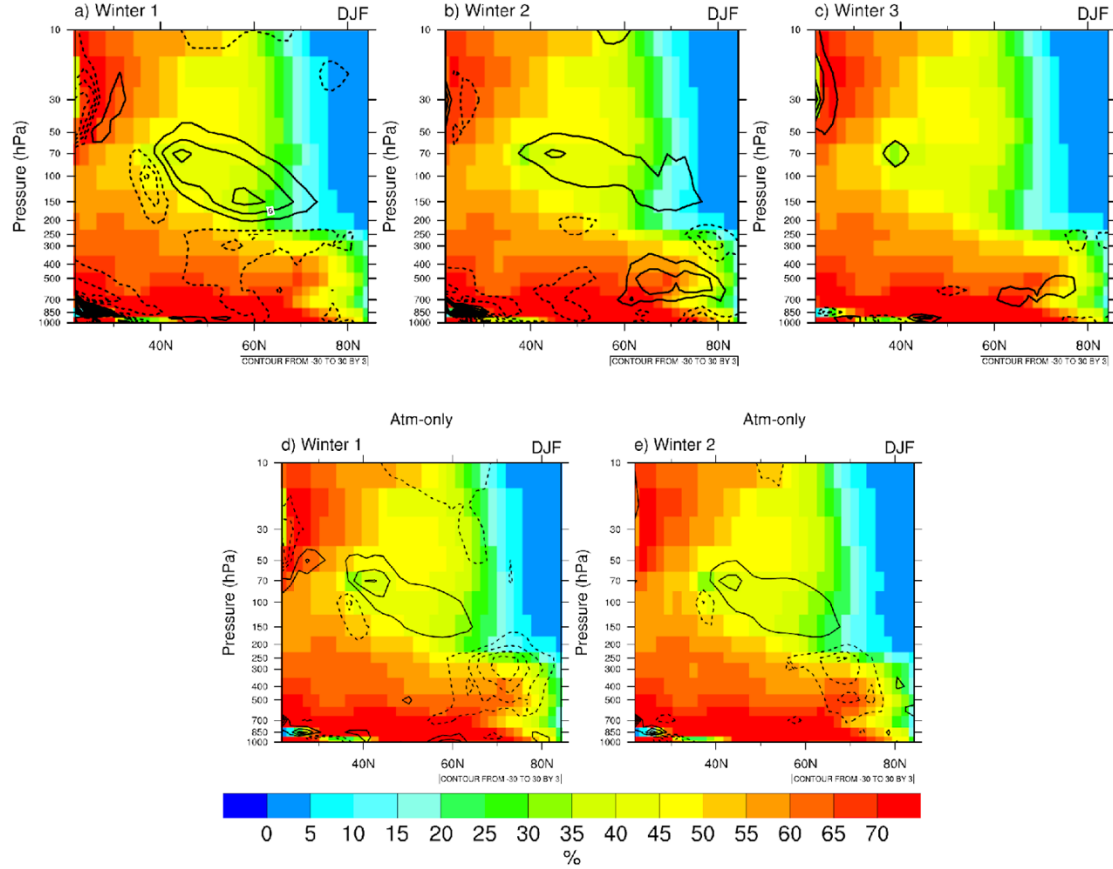
Figure 10. Probability (%) of favorable propagation conditions for large-scale stationary Rossby waves (zonal and meridional wavenumbers 1, 2 and 3) as a function of latitude and pressure levels (shading). Contours show the response in long_summer versus control. a) Winter 1 in *cpl*. b) Winter 2 in *cpl*. c) Winter 3 in *cpl*. d) Winter 1 in *atm-only*. e) Winter 2 in *atm-only*.

The vertical component of the the Plumb flux at 850 hPa (Fig. 8d-f) allows us to locate the origins of the upward EP flux in *cpl* (Fig. 4d-f). It is strongest over the north eastern part of the Pacific Ocean (off the west coast of North America) in winter 1, where it continues up into the lower stratosphere at 150 hPa (see Fig. S1a). In winter 2, the Plumb flux has decreased in the North Pacific and increased over the North Atlantic and Siberia, pointing to a possible influence of the change in land-sea temperature contrast (Fig. 8e). In addition to this upward flux, we also detect downward wave flux over both the Aleutian and Greenland regions at 850 hPa and over a large area south of 45° N at 150 hPa. This downward Plumb flux is evidence of changes in the planetary wave structure where wave reflection occurs due to the sudden weakening of the zonal winds identified in the U10 (Fig. 3a). In winter 3, the Plumb flux now dominates both at 850 (seen in Fig.

23

523   8f) and 150 hPa (Fig. S1c), where it encircles the polar stratosphere north of 60° N. In line with

524   the weak EP-flux response shown in Fig. 5, the Plumb flux anomalies are generally weak in *atm-*

525   *only* compared to *cpl*, for both winter 1 and 2 (Fig. 9c-d).

526

527   Since upward wave activity depends on wave-mean flow interactions, several factors are at play

528   to explain the strong response in *cpl* vs *atm-only*. First, the change in zonal flow is substantially

529   different between the two pairs of experiments, as shown by the U200 anomalies (Fig. 8g-i and

530   Fig. 9e-f). In the first two winters we observe an intense deepening of the Aleutian low in *cpl* (Fig.

531   8a-b) associated with a large equatorward shift of the subtropical jet over the North Pacific (Fig.

532   8g-h, also seen in the zonal-mean averages of Fig. 4). The change in zonal flow is not as large in

533   *atm-only*, where there is a general decrease of U200 on the poleward side of the subtropical jets,

534   rather than a marked equatorward shift as in *cpl*. This further emphasizes that amplified surface

535   coupling when the ocean is coupled to the atmosphere has a dramatic impact on the amplitude of

536   the tropospheric response. Because the zonal flow acts as a waveguide for large-scale planetary

537   waves, we expect changes in upward wave propagation in the stratosphere. To measure how

538   waveguides change, Fig. 10 shows the probability of favorable propagation conditions for large-

539   scale stationary waves, averaged for zonal wave numbers k=1,2,3 and meridional wave numbers

540   l=1,2,3, as a function of pressure and latitude (see section 2 for more details). Areas of high

541   probability show where large-scale waves preferentially propagate, while low probability regions

542   indicate where linear wave propagation is hampered. Generally, the mid-latitude troposphere is

543   more favorable for wave propagation than the high-latitudes and the stratosphere, consistent with

544   the tendency for stationary waves to propagate upwards and to be deflected towards the equator,

545   in climatology. After injection of the volcanic forcing, both *cpl* and *atm-only* exhibit an increase

546   in the probability for wave propagation between 40 and 60 °N in the lower stratosphere during

547   winter 1 and 2, but the responses in the troposphere are markedly different. In *atm-only*, wave

548   propagation is inhibited in the free troposphere north of 60°N, for both winters 1 and 2 (Fig. 10d-

549   e), which is consistent with the EP-flux anomalies of Fig. 5. This response is absent from *cpl* during

550   winter 1 (Fig. 10a), and opposite during winter 2 when an increase of favorable conditions for

551   wave propagation is diagnosed (Fig. 10b). We also see that the waveguide has greatly reduced in

552   the subtropical troposphere in *cpl* winters 1-2 that favor large-scale waves to be redirected towards

553   the pole. This increase in favorable conditions for wave propagation in the troposphere between

554 60 and 80 °N persists during winter 3 in *cpl* (Fig. 10c), which is a partial and the most likely

555 explanation for enhanced upward wave propagation in the stratosphere described in Fig. 4f.

556

557 In *cpl* winter 3, when the cooling is reduced in the NH mid-latitudes and has migrated towards the

558 polar regions, which is also evident in the SST (Fig. 5S), the amplitude of the 850 hPa upward

559 Plumb flux anomalies decreases compared to previous winters (Fig. 8f). This suggests that the

560 mid-latitude spatiotemporal cooling pattern plays a part in the strong wave activity detected near

561 the surface. This can be revealed by computing the T2m gradient (Tgrad) where strong land-sea

562 temperature gradients are known for their ability to influence atmospheric wave activity (Hoskins

563 and Valdes, 1990; Brayshaw et al., 2009; He et al., 2014; Wake et al., 2014; Portal et al., 2022). In

564 winter 1 the meridional gradient shows sharp significant changes encircling 45° N (Fig. 11a), with

565 positive (negative) gradient anomalies occurring south (north) of 45° N. In winter 2 we still see

566 the gradient present at 45° N but now located over North America and the North Pacific. Winter 3

567 mostly reveals regional anomalies in the Barents-Kara, Greenland-Iceland and the North Pacific

568 regions (Figure 11b-c), occurring over areas of significant sea ice increase (not shown). A sharp

569 Tgrad change throughout the NH at 45° N is identified in winter 1 (Fig. 11a) that is followed by a

570 reduction of land-sea temperature contrast over eastern Canada and the U.S. in winter 2 (Fig. 11b).

571 This is a known cause of planetary wave enhancement (Portal et al., 2022) and could provide an

572 explanation for the strong surface upward wave flux detected in the second and third post-volcanic

573 winters (Figure 8e-f). Both the zonal and meridional Tgrad components show an increase in the

574 northern part of Alaska that coincides with the region of T2m warming over the Aleutian/Alaska

575 region (Fig. 8a) and the strong upward Plumb flux (Fig. 8d). This warming, in addition to the

576 strong continental cooling over North East America and the general decrease in Tgrad spanning

577 from mid to northern part of North America, might influence this strong Plumb flux anomaly in

578 the North Pacific. Of note, sea-ice extent increases around East Siberia extending into the Chukchi

579 Sea (not shown), highlighting the potential influence of sea ice variability on Tgrad and upward

580 Plumb flux anomalies in the area.

581 Plotting the average Tgrad for various regions against the average number of SSWs for winters 1-

582 3 (Fig. S6), we do see that the strongest Tgrad reduction occurs over the North East US in the

583 second winter, agreeing with the upward Plumb flux over the same region and serving as further

584 evidence for its contribution to the upward EP flux in winter 2. This Tgrad reduction continues

585 into the third winter where we also detected a reduction in the upward Plumb flux over the same

586 area (Fig. 8f). Looking towards the Barents Sea, a clear spatial difference emerges compared to

587 the North East US, where a clear Tgrad increase occurs in winter 3 related to the SSWs. In general

588 less changes are detected between winters in the North West NA and the North Pacific, reflecting

589 the confined cooling over higher latitudes in winter 3 associated with the SSWs.
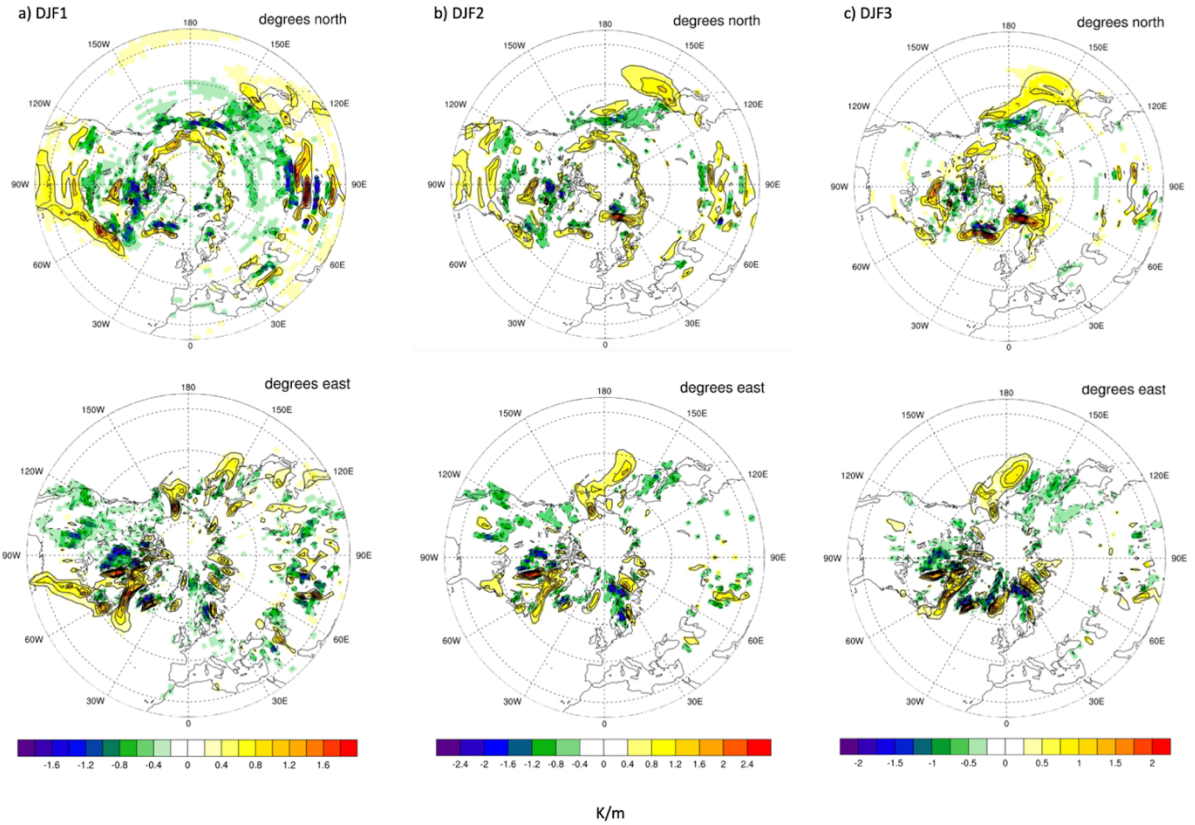
590

591

592 Figure 10: a-c) The zonal (degrees north) and meridional (degrees east) T2m gradient anomalies

593 (perturbed minus unperturbed) for winters 1-3. Contours indicate 95% significance according to a

594 Student's t-test. Note the different colorbar for each winter.

595

596 To complete our assessment of the tropospheric response, we examine if eddies play a role in the

597 *cpl* polar vortex response and the anomalous upward EP flux (Fig. 4a-f) as well as SSWs detected

598 in winter 3 by following Smith et al. (2022) (see Methods). This is done for both perturbed (red)

599 and unperturbed (blue) experiments in *cpl* and *atm-only* (Fig. S4). We see an increase in perturbed

600 eddy feedback at around 40-70° N both for *cpl* winter 1 and winters 1-2 in *atm-only* during the

601 polar vortex strengthening (Fig. S4). However, the role of eddies in the polar vortex weakening in

602 winters 2-3 is unclear, especially considering the eddy feedback increase of the control run in

603 winter 2 (Fig. S4b). In general, these results suggest that the signal-to-noise ratio is too small to

604 identify a role for eddy feedback in our experiments.

605

606 **4 Discussion**

607 Our two sets of coupled ocean-atmosphere (*cpl*) and atmosphere-only (*atm-only*) experiments

608 examine the large-scale climate response to an idealized long-lasting NH eruption, where their

609 differences give us valuable insight into the volcanically forced mechanisms at play within the

610 coupled climate system in CESM1. Specifically, we analyzed the first three winters of the *cpl*

611 experiment and used the first two winters of *atm-only* as a comparison to investigate the dynamics

612 that govern the post-eruption stratospheric polar vortex and the associated surface response.

613 Results from the *cpl* experiment show a similar response in the first winter as in the two winters

614 of *atm-only*, with a strengthening of the zonal winds resulting from an aerosol-induced sharp

615 temperature gradient between the mid-latitudes and the pole (Fig. 4a and Fig. 5a). We show that

616 this zonal wind strengthening is not affected by the detected strong upward EP flux, where the LW

617 flux (Fig. 2e-f) supports our conclusions that the polar vortex strengthening is induced by the

618 thermal wind balance. A distinct change to this pattern emerges in *cpl* winter 2 where we detect an

619 SSW-like pattern, with strong negative anomalies emerging in the polar U50 winds and a warming

620 in the T50 field (Fig. 4b). We also detect an LW absorption at high latitudes, that is absent at

621 midlatitudes, where this T50 warming is evident of the potential role of a decreased temperature

622 gradient in the identified polar vortex weakening. Furthermore, the upward wave-activity flux

623 from the troposphere into the stratosphere and the T50 warming indicate absorption of upward

624 propagating waves into the stratosphere that causes this warming and weakening of U10 winds

625 over the polar cap. This pattern is known to be related to SSWs (Kretschmer et al., 2018; Kodera

626 et al., 2016) that we further confirm to occurr in winter 3. The strong upward EP flux greatly

627 depends on ocean-atmosphere coupling originating in the surface cooling in addition to the

628 changes in upper tropospheric zonal flow. This further contributes to the upward EP flux from the

629 troposphere into the stratosphere that eventually leads to polar vortex weakening and enhanced

630 SSWs.

631 Although the above coincides with a positive (negative) eddy feedback in the first (second) winter

632 that could in theory play a role in sustaining the strengthening (weakening) of the polar vortex, our

27

eddy feedback results indicate low signal-to-noise ratio where further studies with additional ensemble members would be required to confirm their role in the forced response. We also note that Smith et al. (2022) identified CESM1 WACCM-SC as having one of the weakest eddy feedback of the sixteen models they investigated, so the response of eddy feedback may be more significant in other models. Similar to the eddy feedback, low signal-to-noise ratio is also evident in the SSW analysis. However, the response we detect in the U50 and T50 fields is strong compared to the unperturbed simulation where the SSWs provide an explanation in agreement with the patterns detected. Furthermore, the SSW analysis for *atm-only* and the ensemble size test (Fig. 7) both show strong evidence of a robust signal for winter 3 despite the noisy polar vortex and the limited ensemble size. We also see that the large decrease in SSWs in the perturbed simulation of *atm-only* (when compared to unperturbed) is consistent with the detected polar vortex strengthening. This further supports the significance of the signal we detect in *cpl* winter 3 compared to the background noise. In addition, all winters examined, in both *cpl* and *atm-only*, showed that there is up to 15% chance of getting more than 1 SSWs per winter in all ensemble members. This is not far from Ineson et al. (2022) who identified a double event once every 9 years in a 66-year ERA5 record. The exception is *cpl* winter 3 that is also the only winter that has 3 SSWs, with the average SSW occurrence also being the only winter above 1 (1.17) while all other winters span between 0.15-0.85 per winter. A similar NH high-latitude eruption has not taken place during the observational period, so we have no comparison. Also, to the best of our knowledge, a similar high-latitude sulfur injection study has not been performed before. Therefore, it is difficult to say at this stage if such a response is realistic or not, but in general more than two SSWs per winter can be considered exceptional yet plausible, as is also the case for our idealized eruption.

Bittner et al. (2016b) identified an opposite response driven by a similar underlying mechanism, when compared to our *cpl* response in winters 2-3 (Fig. 4), following a Tambora-like eruption where a strengthening of the polar vortex due to less wave breaking at high latitudes was considered to be an indirect effect associated with a changes in planetary wave propagation. Since the volcanic aerosols in our experiments have declined extensively in the third winter, making the aerosol thermal forcing a limited factor, we cannot rule out similar indirect effects where changes in wave propagation leads to an increase in wave breaking at high latitudes and hence the increase in SSWs.

While not directly comparable to our study but still providing an important analog, Muthers et al.
(2016) identified an average increase in the number of SSWs during a 30-year (constant) decrease
in solar radiation in line with our significant increase in SSWs in winter 3. Our results do support
the findings of Sjolte et al. (2019), where the stratospheric temperature gradient does not appear
to play a major role in the polar vortex weakening we identify, while the upward wave flux does.
The strong surface cooling detected in Fig. 8 is a well-known caveat in CMIP5 models (including
CESM1) (Driscoll et al., 2012; Chylek et al., 2020) and is clearly detected in our coupled
simulations. Since our results indicate the dominant role of the volcanically induced stratospheric
thermal wind response that causes the polar vortex strengthening, the cooling does not appear to
impact the response identified in winter 1. This is also revealed by the EP flux. The same cannot
be said about winters 2-3, where our results indicate that the exaggerated spatiotemporal T2m
pattern might explain the strong upward wave flux and the associated stratospheric response.
Interestingly, a slight difference between *atm-only* and *cpl* is detected in both the LW and SW flux
that is caused by a strong significant decrease in high cloud cover in the *cpl* simulation (not shown).
This cloud cover decrease, especially at mid- to high latitudes, agrees with the increased LW fluxes
at higher latitudes in addition to the decrease in SW flux and the associated surface cooling. This
raises a question regarding the role of forced surface processes in these high cloud changes, which
we leave open for further studies.

As mentioned in the methods section, we assume a similar lifetime of volcanic aerosols at 65° N
as at 45° N. When considering the e-folding time in Toohey et al. (2019), a substantial aerosol
decrease of about 43% occurs at 17km (a.b.s.) for an eruption at 60° compared to at 0°. However,
since our experiment assumes a constant stratospheric injection over 5 months with the aim to
simulate a long-lasting HL eruption compared to a single injection at low latitudes, the difference
in the e-folding time between low and high-latitudes would be expected to decrease. Using
CESM2-WACCM6 with interactive chemistry Zhuo et al. (2023) identified that although an
eruption at 64° N did have a shorter aerosol lifetime compared to one at 15° N, it leads to stronger
volcanic forcing over the NH extratropics. In addition, one of their conclusions was that different
duration and intensity of both tropical and NH extratropical eruptions can lead to different results,
stressing that our 6 month long stratospheric sulfate aerosol enhancement is not directly
comparable with volcanic eruptions of shorter duration. Although the aerosol lifetime in our

695 experiment might be exaggerated into the third year, our results do indicate that the polar vortex
696 weakening in winter 2 appears to act as a trigger for further weakening that eventually leads to
697 SSWs in winter 3. In order to increase confidenceprecu on such a delayed link, additional
698 sensitivity simulations are required, which we we leave that for future studies.
699
700 Unlike our eruption simulated using a version of WACCM4, where the chemistry is prescribed,
701 natural volcanic eruptions can contain various chemical compounds that impact the formation and
702 the lifetime of sulfate aerosols as well as affect the atmospheric circulation via, e.g., ozone
703 depletion, like halogens are known to do. More advanced versions as well as models that include
704 interactive chemistry are thus important to reveal in more detail the chemistry-climate interactions
705 that occur in the natural world (Clyne et al., 2021; Case et al., 2023; Fuglestvedt et al., 2024). Thus
706 our idealized experiment can be considered primitive in the sense that it only considers sulfate
707 aerosols but sufficient when focusing on answering questions on the basic mechanism that such
708 eruptions can initiate. Another important aspect that we do not focus on in our study is the role of
709 different initial conditions on the forced climate response, where initial atmospheric and climate
710 conditions, including e.g. the stability of the polar vortex, control the lifetime and distribution of
711 the volcanic aerosols as well as the forced dynamic climate response (Zanchettin et al., 2019;
712 Weierbach et al., 2023; Zhuo et al., 2023; Fuglestvedt et al., 2024). An exception is our assessment
713 on how the easterly and westerly phase of the QBO affect our results where we compared ensemble
714 members showing easterly phase with the westerly ones to test if the U50 and T50 response
715 patterns would be different. They were not: both phases showed a weakening of the U50 although
716 the zonal winds were more confined and consistent over the higher latitudes of the NH during the
717 easterly phase (not shown). The difference in the number of ensemble members used for these
718 calculations could of course impact the statistics of this test of ours but not the overall pattern
719 detected.
720 CESM2-WACCM6 has obvious improvements when compared to CESM1-WACCM4 (see e.g.
721 Gettleman et al., 2019, Danabasoglu et al., 2020), among them being an interactive QBO as well
722 as having a slightly higher frequency of SSW occurrence (Holland et al., 2024). Nonetheless,
723 CESM1-WACCM4 has comparable transient climate response to CESM2 as well as the ability to
724 capture the general physical mechanism occurring within the climate system as identified in

725   various recent studies (Danabasoglu et al., 2020; Zang et al., 2018; Elsbury et al., 2021b; Peings

726   et al., 2023; Ding et al., 2023; Yu et al., 2024).

727

728   **5 Conclusions**

729   Through comparison of the *cpl* and *atm-only* simulations, our results clearly demonstrates the

730   important role of ocean-atmosphere coupling in the stratospheric response to enhancements of the

731   stratospheric sulfate aerosol layer at higher NH latitudes. We see that this aerosol enhancement

732   layer triggers two competing mechanisms in the first three winters:

733   i) Winter 1: The stratospheric polar vortex strengthening is triggered by stratospheric aerosol

734   thermal forcing via thermal wind balance. This response is not influenced by the strong upward

735   wave flux identified, originating in the forced surface cooling and changes in tropospheric

736   circulation, and provides strong evidence of two mechanisms that are competing simultaneously:

737   A Top-down and a Bottom-up mechanism, where the Top-down mechanism dominates the

738   response.

739   ii) Winter 2: The upward wave flux is absorbed in the stratosphere that causes a warming over the

740   polar cap and a polar vortex weakening. This pattern is similar to SSWs although its occurrence is

741   not significant. Here the Bottom-up mechanism dominates.

742   iii) Winter 3: The persistence of the upward wave flux continuing into the third winter leads to an

743   increase in SSWs with warming now confined over the polar cap, again demonstrating the

744   dominating Bottom-up mechanism as in winter 2.

745   It is clear from our results that the strong surface cooling following the HL sulphate aerosol

746   injection causes dramatic changes in tropospheric circulation. These changes further modify

747   atmospheric waveguides where we detect an increase in propagation of planetary waves in the

748   lower stratosphere occurring at higher latitudes. Although we do find similarities in the eddy

749   feedback when compared to the general climate signal that we identify, such as the decrease in

750   eddy feedback in winter 1 potentially sustaining the polar vortex strengthening, we emphasize its

751   weak signal. At the same time we encourage further studies on this subject, especially concerning

752   the lack of published comparison studies regarding both high and low latitude volcanic eruptions

753   and SSWs. Ideally such studies would include the latest model generations in addition to

754   observational datasets. They should also consider the impact of different climate realizations and

755   the eruption magnitude on the forced response. Furthermore, these results highlight the importance

756 of including high-latitude volcanic forcing simulations of various lengths and/or magnitudes in
757 projects such as VolMIP, especially considering the current volcanic unrest and increased activity
758 in some of the major volcanic systems in Iceland.
759 Currently, work is ongoing to test the sensitivity of the polar vortex and the emerging SSWs to NH
760 eruptions that are smaller in magnitude as well as the long-term climate impacts.
761

Data availability

763 The model output is available upon request by contacting the corresponding author.
764

Author contribution

766 HG conceptualized this study along with GM, YP and DZ. *cpl* and *atm-only* experiments were
767 carried out by HG and YP. Analysis and calculations of model output as well as graphical
768 representation was done by HG except for the eddy feedback and the probability of favorable
769 propagation conditions that was done by YP and the ensemble size test that was done by DZ.
770 Manuscript draft was done by HG and editing was done by DZ and YP. GM served as the principal
771 investigator of this work and did the final editing.
772

773

Competing interests

775 The corresponding author declares that none of the authors have any competing interest.
776

References

787

788

789

790 **References**

791 Azoulay, A., Schmidt, H., & Timmreck, C.. The Arctic polar vortex response to volcanic forcing

792 of different strengths. *J Geophys Res-Atmos*, *126*(11), e2020JD034450 (2021).

793

794 Baldwin, M. P., & Dunkerton, T. J. Propagation of the Arctic Oscillation from the stratosphere to

795 the troposphere. *J Geophys Res-Atmos*, *104*(D24), 30937-30946 (1999).

796

797 Barsotti, S., Di Rienzo, D. I., Thordarson, T., Björnsson, B. B., & Karlsdóttir, S. Assessing impact

798 to infrastructures due to tephra fallout from Öræfajökull volcano (Iceland) by using a scenario-

799 based approach and a numerical model. *Front Earth Sci, 6*, 196 (2018).

800

801 Bittner M, Schmidt H, Timmreck C, Sienz F. Using a large ensemble of simulations to assess the

802 Northern Hemisphere stratospheric dynamical response to tropical volcanic eruptions and its

803 uncertainty. *Geophys Res Lett*., 43(17), 9324–32 (2016).

804

805 Brayshaw, D. J., B. Hoskins, and M. Blackburn. The basic ingredients of the North Atlantic storm

806 track. Part I: Land–sea contrast and orography. *J. Atmos. Sci.*, **66**, 2539–2558,

807 https://doi.org/10.1175/2009JAS3078.1 (2009).

808

809 Brown, F., Marshall, L., Haynes, P. H., Garcia, R. R., Birner, T., & Schmidt, A. On the magnitude

810 and sensitivity of the quasi-biennial oscillation response to a tropical volcanic eruption. *Atmos.*

811 *Chem. Phys*, *23*(9), 5335-5353 (2023).

812

813 Brugnatelli, V., & Tibaldi, A. Effects in North Africa of the 934–940 CE Eldgjá and 1783–1784

814 CE Laki eruptions (Iceland) revealed by previously unrecognized written sources. *B. Volcanol*,

815 *82*(11), 73 (2020).

816

817   Case, P., Colarco, P. R., Toon, B., Aquila, V., & Keller, C. A. Interactive stratospheric aerosol
818   microphysics-chemistry simulations of the 1991 Pinatubo volcanic aerosols with newly coupled
819   sectional aerosol and stratosphere-troposphere chemistry modules in the NASA GEOS Chemistry-
820   Climate Model (CCM). *J Adv. Model Earth Sy.*, *15*(8), e2022MS003147 (2023).

821

822   Charlton-Perez AJ, Ferranti L, Lee RW. The influence of the stratospheric state on North Atlantic
823   weather regimes. Quart. J. Roy. Meteor. Soc, 144:1140–1151. https://doi.org/10.1002/qj.3280
824   (2018).

825   Charlton, A. J., & Polvani, L. M. A new look at stratospheric sudden warmings. Part I: Climatology
826   and modeling benchmarks. *J. Climate*, *20*(3), 449-469 (2007).

827

828   Church, J.A., White, N.J., Arblaster, J.M. Significant decadal-scale impact of volcanic eruptions
829   on sea level and ocean heat content. *Nature* 438 (7064), 74–77 (2005).

830

831   Chylek, P., Folland, C., Klett, J. D., & Dubey, M. K. CMIP5 climate models overestimate cooling
832   by volcanic aerosols. *Geophys. Res. Lett*, *47*(3), e2020GL087047 (2020).

833

834   Clyne, M., Lamarque, J.-F., Mills, M. J., Khodri, M., Ball, W., Bekki, S., Dhomse, S. S., Lebas,
835   N., Mann, G., Marshall, L., Niemeier, U., Poulain, V., Robock, A., Rozanov, E., Schmidt, A.,
836   Stenke, A., Sukhodolov, T., Timmreck, C., Toohey, M., Tummon, F., Zanchettin, D., Zhu, Y., and
837   Toon, O. B.: Model physics and chemistry causing intermodel disagreement within the VolMIP-
838   Tambora Interactive Stratospheric Aerosol ensemble, Atmos. Chem. Phys., 21, 3317–3343,
839   https://doi.org/10.5194/acp-21-3317-2021, (2021).

840

841   Colose CM, LeGrande AN, Vuille M. Hemispherically asymmetric volcanic forcing of tropical
842   hydroclimate during the last millennium. *Earth Sys Dyn*. 7(3), 681–96. doi:10.5194/esd-7-681-
843   2016 (2016).

844

845   DallaSanta, K., Gerber, E. P., & Toohey, M. The circulation response to volcanic eruptions: The
846   key roles of stratospheric warming and eddy interactions. *J. Clim*, *32*(4), 1101-1120 (2019).

847

848 DallaSanta, K., & Polvani, L. M. Volcanic stratospheric injections up to 160 Tg (S) yield a Eurasian

849 winter warming indistinguishable from internal variability. *Atm. Chem. Phys*, *22*(13), 8843-8862

850 (2022).

851

852 Danabasoglu, G., Lamarque, J. F., Bacmeister, J., Bailey, D. A., DuVivier, A. K., Edwards, J., ...

853 & Strand, W. G. The community earth system model version 2 (CESM2). *J Adv. Model Earth*

854 *Sy, 12*(2), e2019MS001916 (2020).

855

856 Dee, S. G., Cobb, K. M., Emile-Geay, J., Ault, T. R., Edwards, R. L., Cheng, H., & Charles, C. D.

857 No consistent ENSO response to volcanic forcing over the last millennium. *Science*, *367*(6485),

858 1477-1481 (2020).

859

860 Ding, X., Chen, G., Zhang, P., Domeisen, D. I., & Orbe, C. Extreme stratospheric wave activity as

861 harbingers of cold events over North America. *Commun. Earth Environ*, *4*(1), 187 (2023).

862

863 Domeisen, D. I., Grams, C. M., & Papritz, L. The role of North Atlantic–European weather regimes

864 in the surface impact of sudden stratospheric warming events. *Weather Clim. Dynam*, *1*(2), 373-

865 388 (2020).

866

867 Driscoll, S., Bozzo, A., Gray, L. J., Robock, A., Stenchikov, G. Coupled ModelIntercomparison

868 Project 5 (CMIP5) simulations of climate following volcanic erup-tions. *J. Geophys. Res-Atmos,*

869 117 (D17) (2012).

870

871 Edmon, H.J., Hoskins, B.J. and McIntyre, M.E. Eliassen-Palm cross sections for the troposphere.

872 *J. Atmos. Sci*, **37**, 2600–2616 (1980).

873

874 Einarsson, P. Historical accounts of pre-eruption seismicity of Katla, Hekla, Öræfajökull and other

875 volcanoes in Iceland. *Jökull*, *69*, 35-52 (2019).

876

877 Elsbury, D., Y. Peings and G. Magnusdottir. Variation in the Holton-Tan effect by longitude. Q. J.
878 Roy. Meteor. Soc. DOI: 10.1002/qj.3993 (2021b).

879

880 Elsbury, D., Peings, Y., & Magnusdottir, G. CMIP6 models underestimate the Holton-Tan effect.
881 *Geophys. Res. Lett*, *48*(24), e2021GL094083 (2021).

882

883 Fischer, H., Siggaard-Andersen, M.L., Ruth, U., Röthlisberger, R., Wolff, E. Glacial/interglacial
884 changes in mineral dust and sea-salt records in polar ice cores: Sources,transport, and deposition.
885 *Rev. Geophys*. (1), 45 (2007).

886

887 Fuglestvedt, H. F., Zhuo, Z., Toohey, M., & Krüger, K. Volcanic forcing of high-latitude Northern
888 Hemisphere eruptions. *npj Clim. Atmos. Sci*, *7*(1), 10 (2024).

889

890 Gettelman, A., Mills, M. J., Kinnison, D. E., Garcia, R. R., Smith, A. K., Marsh, D. R., ... & Randel,
891 W. J. The whole atmosphere community climate model version 6 (WACCM6). *J. Geophys. Res-*
892 *Atmos*, *124*(23), 12380-12403 (2019).

893

894 Gettelman, A., Schmidt, A., & Egill Kristjánsson, J. Icelandic volcanic emissions and climate.
895 *Nature Geosci*, *8*(4), 243-243 (2015).

896

897 Gleckler, P.J., AchutaRao, K., Gregory, J.M., Santer, B.D., Taylor, K.E., Wigley, T.M.L. Krakatoa
898 lives: The effect of volcanic eruptions on ocean heat content and thermal expansion. Geophys. Res.
899 Lett. (17), 33 (2006).

900

901 Graf, H.F., Perlwitz, J., Kirchner, I. Northern hemisphere tropospheric midlatitude circulation after
902 violent volcanic eruptions. Contr. Atmos. Physics 67 (1), 3–13 (1994).

903

904 Graf, H.-F., D. Zanchettin, C. Timmreck and M. Bittner. Observational constraints on the
905 tropospheric and near-surface winter signature of the Northern Hemisphere stratospheric polar
906 vortex. Clim. Dyn., 43, 3245, doi:10.1007/s00382-014-2101-0 (2014).

907

908   Guðlaugsdóttir, H., Steen-Larsen, H. C., Sjolte, J., Masson-Delmotte, V., Werner, M., &

909   Sveinbjörnsdóttir, Á. E. The influence of volcanic eruptions on weather regimes over the North

910   Atlantic simulated by ECHAM5/MPI-OM ensemble runs from 800 to 2000 CE. *Atm. Res*, *213*,

911   211-223 (2018).

912

913   Guðlaugsdóttir, H., Sjolte, J., Sveinbjörnsdóttir, Á. E., Werner, M., & Steen-Larsen, H. C. North

914   Atlantic weather regimes in δ18O of winter precipitation: isotopic fingerprint of the response in

915   the atmospheric circulation after volcanic eruptions. *Tellus B*, *71*(1), 1633848 (2019).

916

917   Haynes, P. H. Stratospheric dynamics. *Ann. Rev. Fluid Mech. 37(1), 263-293, doi:*

918   *10.1146/annurev.fluid.37.061903.175710* (2005).

919

920   He, Y., Huang, J. & Ji, M. Impact of land–sea thermal contrast on interdecadal variation in

921   circulation and blocking. *Clim Dyn* **43**, 3267–3279, https://doi.org/10.1007/s00382-014-2103-y

922   *(2014).*

923

924   Holland, M. M., Hannay, C., Fasullo, J., Jahn, A., Kay, J. E., Mills, M., ... & Bailey, D. New model

925   ensemble reveals how forcing uncertainty and model structure alter climate simulated across CMIP

926   generations of the Community Earth System Model. *Geosci. Model Dev*, *17*(4), 1585-1602 (2024).

927

928   Hoskins, B. J., and P. J. Valdes. On the existence of storm-tracks. *J. Atmos. Sci.*, **47**, 1854–1864,

929   https://doi.org/10.1175/1520-0469(1990)047<1854:OTEOST>2.0.CO;2 (1990).

930

931   Huang, J., Hitchcock, P., Maycock, A. C., McKenna, C. M., & Tian, W. Northern hemisphere cold

932   air outbreaks are more likely to be severe during weak polar vortex conditions. *Commun. Earth*

933   *Environ*, *2*(1), 147 (2021).

934

935   Hurrell, J.W. Decadal trends in the north atlantic oscillation: regional tempera-tures and

936   precipitation. Science 269 (5224), 676–679 (1995).

937

938 Hurrell, J. W., Holland, M. M., Gent, P. R., Ghan, S., Kay, J. E., Kushner, P. J., ... & Marshall, S.
939 The community earth system model: a framework for collaborative research. *B. Am. Meteorol.*
940 *Soc*, *94*(9), 1339-1360 (2013).

941

942 Ineson, S., Dunstone, N. J., Scaife, A. A., Andrews, M. B., Lockwood, J. F., & Pang, B. Statistics
943 of sudden stratospheric warmings using a large model ensemble. *Atmos. Sci. Lett*, *25*(3), e1202
944 (2024).

945

946 Jungclaus, J. H., Bard, E., Baroni, M., Braconnot, P., Cao, J., Chini, L. P., Egorova, T., Evans, M.,
947 González-Rouco, J. F., Goosse, H., Hurtt, G. C., Joos, F., Kaplan, J. O., Khodri, M., Klein
948 Goldewijk, K., Krivova, N., LeGrande, A. N., Lorenz, S. J., Luterbacher, J., Man, W., Maycock,
949 A. C., Meinshausen, M., Moberg, A., Muscheler, R., Nehrbass-Ahles, C., Otto-Bliesner, B. I.,
950 Phipps, S. J., Pongratz, J., Rozanov, E., Schmidt, G. A., Schmidt, H., Schmutz, W., Schurer, A.,
951 Shapiro, A. I., Sigl, M., Smerdon, J. E., Solanki, S. K., Timmreck, C., Toohey, M., Usoskin, I. G.,
952 Wagner, S., Wu, C.-J., Yeo, K. L., Zanchettin, D., Zhang, Q., and Zorita, E.: The PMIP4
953 contribution to CMIP6 – Part 3: The last millennium, scientific objective, and experimental design
954 for the PMIP4 past1000 simulations, Geosci. Model Dev., 10, 4005-4033,
955 https://doi.org/10.5194/gmd-10-4005-2017, (2017).

956

957 Karami, K., Braesicke, P., Sinnhuber, M., and Versick, S. On the climatological probability of the
958 vertical propagation of stationary planetary waves, Atmos. Chem. Phys., 16, 8447–8460,
959 https://doi.org/10.5194/acp-16-8447-2016 (2016).

960

961 Khodri, M., Izumo, T., Vialard, J., Janicot, S., Cassou, C., Lengaigne, M., et al. Tropical explosive
962 volcanic eruptions can trigger El Niño by cooling tropical Africa. Nat. Commun, 8(1), 778.
963 https://doi.org/10.1038/s41467-017-00755-6 (2017).

964

965 Kim, B.M., Son, S.W., Min, S.K., Jeong, J.H., Kim, S.J., Zhang, X., Shim, T., Yoon, J.H.
966 Weakening of the stratospheric polar vortex by arctic sea-ice loss. Nat.Commun. 5, 4646 (2014).

967

Kodera, K. Influence of volcanic eruptions on the troposphere through strato-spheric dynamical processes in the northern hemisphere winter. J. Geophys. Res.-Atmos. 99 (D1), 1273–1282 (1994).

Kodera, K., Mukougawa, H., Maury, P., Ueda, M., & Claud, C. Absorbing and reflecting sudden stratospheric warming events and their relationship with tropospheric circulation. *J. Geophys. Res-Atmos*, *121*(1), 80-94 (2016).

Kolstad, E. W., Lee, S. H., Butler, A. H., Domeisen, D. I., & Wulff, C. O. Diverse surface signatures of stratospheric polar vortex anomalies. *J. Geophys. Res-Atmos*, *127*(20), e2022JD037422 (2022).

Kretschmer, M., Cohen, J., Matthias, V., Runge, J., & Coumou, D. The different stratospheric influence on cold-extremes in Eurasia and North America. *npj Clim. Atmos. Sci*, *1*(1), 44 (2018).

Labe, Z., Peings, Y., & Magnusdottir, G. The effect of QBO phase on the atmospheric response to projected Arctic sea ice loss in early winter. *Geophys. Res. Lett.*, *46*(13), 7663-7671 (2019).

Larsen, G., & Gudmundsson, M. T. Volcanic system: Bárðarbunga system. *Catalogue of Icelandic Volcanoes*, 1-11 (2014).

Lehtonen, I., & Karpechko, A. Y. Observed and modeled tropospheric cold anomalies associated with sudden stratospheric warmings. *J. Geophys. Res-Atmos.*, *121*(4), 1591-1610 (2016).

Ma, J., Chen, W., Yang, R. et al. Downward propagation of the weak stratospheric polar vortex events: the role of the surface arctic oscillation and the quasi-biennial oscillation. Clim. Dyn. 62, 4117–4131 https://doi.org/10.1007/s00382-024-07121-5 (2024).

Matsuno, T. Vertical propagation of stationary planetary waves in the winter Northern Hemisphere, J. Atmos. Sci., 27, 871–883. 32291, 32292, 32294, 32296, 32306 (1970).

Meronen, H., Henriksson, S. V., Räisänen, P., & Laaksonen, A. Climate effects of northern hemisphere volcanic eruptions in an Earth System Model. *Atmos. Res.*, *114*, 107-118 (2012).

999

1000 Muthers, S., Raible, C. C., Rozanov, E., & Stocker, T. F. Response of the AMOC to reduced solar

1001 radiation–the modulating role of atmospheric chemistry. *Earth Syst. Dynam.*, *7*(4), 877-892

1002 (2016).

1003

1004 Nakamura, N. Large-Scale Eddy-Mean Flow Interaction in the Earth's Extratropical

1005 Atmosphere. *Annu. Rev. Fluid Mech.*, *56*(1), 349-377 (2024).

1006

1007 Neely III, R. R., Conley, A. J., Vitt, F., & Lamarque, J. F. A consistent prescription of stratospheric

1008 aerosol for both radiation and chemistry in the Community Earth System Model (CESM1). *Geosci.*

1009 *Model Dev.*, *9*(7), 2459-2470 (2016).

1010

1011 Oman, L., Robock, A., Stenchikov, G., Schmidt, G. A., & Ruedy, R. Climatic response to high-

1012 latitude volcanic eruptions. *J. Geophys. Res-Atmos*, *110*(D13) (2005).

1013

1014 Omrani, N.-E., Keenlyside, N., Matthes, K., Boljka, L., Zanchettin, D., Jungclaus, J. H., Lubis, S.

1015 W. Coupled stratosphere-troposphere-Atlantic multidecadal oscillation and its importance for

1016 near-future climate projection. *npj Clim. Atmos. Sci*, 5, 59, https://doi.org/10.1038/s41612-022-

1017 00275-1 (2022).

1018

1019 Oppenheimer, C., Orchard, A., Stoffel, M., Newfield, T. P., Guillet, S., Corona, C., ... & Büntgen,

1020 U. The Eldgjá eruption: timing, long-range impacts and influence on the Christianisation of

1021 Iceland. *Climatic Change*, *147*, 369-381.Otterå, O.H., Bentsen, M., Drange, H., Suo, L., 2010.

1022 External forcing as a metronome foratlantic multidecadal variability. Nat. Geosci. 3 (10), 688–694

1023 (2018).

1024

1025 Ortega, P., Swingedouw, D., Masson-Delmotte, V., Risi, C., Vinther, B., Yiou, P., Vautard,R.,

1026 Yoshimura, K. Characterizing atmospheric circulation signals in. Greenlandice cores: insights

1027 from a weather regime approach. Clim. Dyn. 43 (9–10), 2585–2605 (2014).

1028

1029   Otterå, O. H., Bentsen, M., Drange, H., & Suo, L. External forcing as a metronome for Atlantic

1030   multidecadal variability. *Nat. Geosci*, *3*(10), 688-694 (2010).

1031

1032   Pausata, F. S. R., Chafik, L., Caballero, R. & Battisti, D. S. Impacts of high- latitude volcanic

1033   eruptions on ENSO and AMOC. Proc. Natl Acad. Sci. 112, 13784–13788 (2015).

1034

1035   Pausata, F.S.R., Zanchettin, D., Karamperidou, C., Caballero, R., Battisti, D. S. ITCZ shift and

1036   extratropical teleconnections drive ENSO response to volcanic eruptions. Sci. Adv. 6(23)

1037   eaaz5006, doi: 10.1126/sciadv.aaz5006 (2020).

1038

1039   Pausata, F. S. R., Zhao, Y., Zanchettin, D., Caballero, R., & Battisti, D. S. Revisiting the

1040   mechanisms of ENSO response to tropical volcanic eruptions. Geophys. Res. Lett., 50,

1041   e2022GL102183. https://doi.org/10.1029/2022GL102183 (2023).

1042

1043   Perlwitz, J., Graf, H.F. The statistical connection between tropospheric and. stra-tospheric

1044   circulation of the Northern Hemisphere in winter. J. Clim. (10),2281–2295 (1995).

1045

1046   Peings, Y., & Magnusdottir, G. Response of the wintertime Northern Hemisphere atmospheric

1047   circulation to current and projected Arctic sea ice decline: A numerical study with CAM5. *J. Clim.*,

1048   *27*(1), 244-264 (2014).

1049

1050   Peings, Y., Davini, P., & Magnusdottir, G. Impact of Ural blocking on early winter climate

1051   variability under different Barents-Kara sea ice conditions. *J. Geophys. Res-Atmos*, *128*(6),

1052   e2022JD036994 (2023).

1053

1054   Plumb, R. A. On the three-dimensional propagation of stationary waves. *J. Atmos. Sci.*, *42*(3), 217-

1055   229 (1985).

1056

1057   Polvani, L. M., Banerjee, A., & Schmidt, A. Northern Hemisphere continental winter warming

1058   following the 1991 Mt. Pinatubo eruption: reconciling models and observations. *Atmos. Chem.*

1059   *Phys*, *19*(9), 6351-6366 (2019).

1060

Portal, A., Pasquero, C., D'andrea, F., Davini, P., Hamouda, M. E., & Rivière, G. Influence of reduced winter land–sea contrast on the midlatitude atmospheric circulation. *J. Clim.*, *35*(19), 6237-6251 (2022).

Predybaylo, E., Stenchikov, G., Wittenberg, A. T. & Osipov, S. El Niño/ Southern Oscillation response to low-latitude volcanic eruptions depends on ocean pre-conditions and eruption timing. Commun. Earth Environ. 1, 1–13 (2020).

Rayner, N. A. A., Parker, D. E., Horton, E. B., Folland, C. K., Alexander, L. V., Rowell, D. P., ... & Kaplan, A. Global analyses of sea surface temperature, sea ice, and night marine air temperature since the late nineteenth century. *J. Geophys. Res-Atmos*, *108*(D14) (2003).

Robock, A., Mao, J. Winter warming from large volcanic eruptions. Geophys. Res.Lett. 19 (24), 2405–2408 (1992).

Robock, A. Volcanic eruptions and climate. Rev. Geophys. 38 (2), 191–219 (2000).

Screen, J. A., Deser, C., Smith, D. M., Zhang, X., Blackport, R., Kushner, P. J., ... & Sun, L. Consistency and discrepancy in the atmospheric response to Arctic sea-ice loss across climate models. *Nat. Geosci.*, *11*(3), 155-163 (2018).

Shindell, D.T., Schmidt, G.A., Mann, M.E., Faluvegi, G. Dynamic winter. Climate response to large tropical volcanic eruptions since 1600. J. Geophys. Res.-Atmos.(D5), 109.Sigl, M., Winstrup, M., McConnell, J.R., Welten, K.C., Plunkett, G., Ludlow, F., Buntgen,U., Caffee, M., Chellman, N., Dahl-Jensen, D., Fischer, H., 2009. Timing and climate forcing of volcanic eruptions for the past 2500 years. Nature 523 (7562), 543–549 (2009).

Sjolte, J., Adolphi, F., Guðlaugsdòttir, H., & Muscheler, R. Major Differences in Regional Climate Impact Between High-and Low-Latitude Volcanic Eruptions. *Geophys. Res. Lett.*, *48*(8), e2020GL092017 (2021).

Smith, D. M., Eade, R., Andrews, M. B., Ayres, H., Clark, A., Chripko, S., ... & Walsh, A. Robust but weak winter atmospheric circulation response to future Arctic sea ice loss. *Nat. Commun.*, *13*(1), 727 (2022)..

Smith, K. L., Neely, R. R., Marsh, D. R., & Polvani, L. M. The specified chemistry whole atmosphere community climate model (SC-WACCM). *J Adv. Model Earth Sy*, *6*(3), 883-901 (2014).

Stenchikov, G., Robock, A., Ramaswamy, V., Schwarzkopf, M.D., Hamilton, K.,Ramachandran, S. Arctic Oscillation response to the 1991 Mount Pinatubo.eruption: Effects of volcanic aerosols and ozone depletion. J. Geophys. Res.-Atmos.(D24), 107 (2002).

Stenchikov, G., Delworth, T.L., Ramaswamy, V., Stouffer, R.J., Wittenberg, A., Zeng, F. Volcanic signals in oceans. J. Geophys. Res.-Atmos. (D16), 114 (2009).

Stothers, R. B. Far reach of the tenth century Eldgjá eruption, Iceland. *Climatic Change*, *39*(4), 715-726 (1998).

Swingedouw, D., Ortega, P., Mignot, J., Guilyardi, E., Masson-Delmotte, V., Butler, P.G.,Khodri, M., Séférian, R. Bidecadal North Atlantic ocean circulation variability controlled by timing of volcanic eruptions. Nat. Commun. 6, 6545 (2015).

Thomas, M. A., Giorgetta, M. A., Timmreck, C., Graf, H. F., & Stenchikov, G. Simulation of the climate impact of Mt. Pinatubo eruption using ECHAM5–Part 2: Sensitivity to the phase of the QBO and ENSO. *Atmos. Chem. Phys*, *9*(9), 3001-3009 (2009).

Timmreck, C.: Modeling the climatic effects of large explosive volcanic eruptions, Wiley Interdisciplinary Reviews: Climate Change, 3, 545–564, (2012).

1121   Thordarson, T., & Self, S. Atmospheric and environmental effects of the 1783–1784 Laki eruption:

1122   A review and reassessment. *J. Geophys. Res.-Atmos.*, *108*(D1), AAC-7 (2003).

1123

1124   Thordarson, T., Miller, D. J., Larsen, G., Self, S., & Sigurdsson, H. New estimates of sulfur

1125   degassing and atmospheric mass-loading by the 934 AD Eldgjá eruption, Iceland. *J. Volcanol.*

1126   *Geoth. Res.*, *108*(1-4), 33-54 (2001).

1127

1128   Toohey, M., Stevens, B., Schmidt, H., & Timmreck, C. Easy Volcanic Aerosol (EVA v1. 0): an

1129   idealized forcing generator for climate simulations. *Geosci. Model Dev.*, *9*(11), 4049-4070 (2016).

1130

1131   Toohey, M., Krüger, K., Schmidt, H., Timmreck, C., Sigl, M., Stoffel, M., & Wilson, R.

1132   Disproportionately strong climate forcing from extratropical explosive volcanic eruptions. Nat.

1133   Geosci, 12(2), 100-107 (2019).

1134

1135   Toohey, M., Krüger, K., Bittner, M., Timmreck, C., and Schmidt, H.: The impact of volcanic

1136   aerosol on the Northern Hemisphere stratospheric polar vortex: mechanisms and sensitivity to

1137   forcing structure, Atmos. Chem. Phys., 14, 13063–13079, https://doi.org/10.5194/acp-14-13063-

1138   2014, (2014).

1139

1140   Wake, B. Land–sea contrast. *Nat. Clim. Change* 4, 326 https://doi.org/10.1038/nclimate2233

1141   (2014).

1142

1143   Weierbach, H., LeGrande, A. N., and Tsigaridis, K.: The impact of ENSO and NAO initial

1144   conditions and anomalies on the modeled response to Pinatubo-sized volcanic forcing, Atmos.

1145   Chem. Phys., 23, 15491–15505, https://doi.org/10.5194/acp-23-15491-2023, (2023).

1146

1147   Yu, Q., Wu, B., & Zhang, W. The atmospheric connection between the Arctic and Eurasia is

1148   underestimated in simulations with prescribed sea ice. Commun. Earth Environ., *5*(1), 435 (2024).

1149

1150   Zambri, B., Robock, A., Mills, M. J., & Schmidt, A. Modeling the 1783–1784 Laki eruption in

1151   Iceland: 2. Climate impacts. *J. Geophys. Res.-Atmos*, *124*(13), 6770-6790 (2019).

Zambri B, Slawinska J, Robock A, LeGrande AN. Northern Hemisphere Winter Warming and Summer Monsoon Reduction after Volcanic Eruptions over the Last Millennium. J Geophys Res Atmos, 122 (15) :7971-7989. doi: 10.1002/2017jd026728 (2017).

Zanchettin, D., Timmreck, C., Graf, H.F., Rubino, A., Lorenz, S., Lohmann, K., Jungclaus,J.H. Bi-decadal variability excited in the coupled ocean-atmosphere system by strong tropical volcanic eruptions. Clim. Dyn. 39 (1–2), 419–444 (2012).

Zanchettin, D., Timmreck, C., Bothe, O., Lorenz, S.J., Hegerl, G., Graf, H.F., Lutherbacher,J., Jungclaus, J.H. Delayed winter warming: A robust decadal response to strong tropical volcanic eruptions. Geophys. Res. Lett. 40 (1), 204–209 (2013).

Zanchettin, D., Khodri, M., Timmreck, C., Toohey, M., Schmidt, A., Gerber, E. P., Hegerl, G., Robock, A., Pausata, F. S. R., Ball, W. T., Bauer, S. E., Bekki, S., Dhomse, S. S., LeGrande, A. N., Mann, G. W., Marshall, L., Mills, M., Marchand, M., Niemeier, U., Poulain, V., Rozanov, E., Rubino, A., Stenke, A., Tsigaridis, K., and Tummon, F.: The Model Intercomparison Project on the climatic response to Volcanic forcing (VolMIP): experimental design and forcing input data for CMIP6, Geosci. Model Dev., 9, 2701-2719, doi:10.5194/gmd-9-2701-2016, (2016).

Zanchettin, D., C. Timmreck, M. Toohey, J. H. Jungclaus, M. Bittner, S. J. Lorenz, A. Rubino. Clarifying the Relative Role of Forcing Uncertainties and Initial-Condition Unknowns in Spreading the Climate Response to Volcanic Eruptions. Geophys. Res. Lett. 46, 1602-1611, https://doi.org/10.1029/2018GL081018 (2019).

Zanchettin, D. Aerosol and Solar Irradiance Effects on Decadal Climate Variability and Predictability. Current Climate Change Reports, 3, 150, doi:10.1007/s40641-017-0065-y (2017).

Zanchettin, D., Timmreck, C., Khodri, M., Schmidt, A., Toohey, M., Abe, M., Bekki, S., Cole, J., Fang, S.-W., Feng, W., Hegerl, G., Johnson, B., Lebas, N., LeGrande, A. N., Mann, G. W., Marshall, L., Rieger, L., Robock, A., Rubinetti, S., Tsigaridis, K., and Weierbach, H.: Effects of forcing differences and initial conditions on inter-model agreement in the VolMIP volc-pinatubo-

full experiment, Geosci. Model Dev., 15, 2265–2292, https://doi.org/10.5194/gmd-15-2265-2022, (2022).

Zhang, P., Wu, Y., Simpson, I. R., Smith, K. L., Zhang, X., De, B., & Callaghan, P. A stratospheric pathway linking a colder Siberia to Barents-Kara Sea sea ice loss. *Sci. Adv.*, *4*(7), eaat6025 (2018).

Zhang, R., Tian, W., Zhang, J., Huang, J., Xie, F., & Xu, M. The corresponding tropospheric environments during downward-extending and nondownward-extending events of stratospheric northern annular mode anomalies. *J. Clim*, *32*(6), 1857-1873 (2019).

Zhu, F., Emile-Geay, J., Anchukaitis, K. J., Hakim, G. J., Wittenberg, A. T., Morales, M. S., ... & King, J. A re-appraisal of the ENSO response to volcanism with paleoclimate data assimilation. *Nat. Commun.*, *13*(1), 747 (2022).

Zhuo, Z., Fuglestvedt, H. F., Toohey, M., and Krüger, K.: Initial atmospheric conditions control transport of volcanic volatiles, forcing and impacts, Atmos. Chem. Phys., 24, 6233–6249, https://doi.org/10.5194/acp-24-6233-2024, (2024).